Climate
of the Past

# How temperature seasonality drives interglacial permafrost dynamics: implications for paleo reconstructions and future thaw trajectories

**Jan Nitzbon**[1,2,3], **Moritz Langer**[2,4], **Luca Alexander Müller-Ißberner**[3], **Elisabeth Dietze**[3], and **Martin Werner**[1]

[1]Paleoclimate Dynamics Section, Alfred Wegener Institute Helmholtz Centre for Polar and Marine Research, Bremerhaven, Germany
[2]Permafrost Research Section, Alfred Wegener Institute Helmholtz Centre for Polar and Marine Research, Potsdam, Germany
[3]Institute of Geography, Georg-August-Universiät Göttingen, Göttingen, Germany
[4]Earth sciences, Vrije Universiteit Amsterdam, Amsterdam, the Netherlands

**Correspondence:** Jan Nitzbon (jan.nitzbon@awi.de)

**Abstract.** Various proxy records have suggested widespread permafrost degradation in northern high latitudes during interglacial warm climates, including the mid Holocene (MH, 6000 years before present) and the last interglacial (LIG, 127 ka BP), and linked this to substantially warmer high-latitude climates compared to the pre-industrial period (PI). However, most Earth system models suggest only modest warming or even slight cooling in terms of annual mean surface temperatures during these interglacials, seemingly contradicting the reconstructions of widespread permafrost degradation. Here, we combine paleo climate simulations of the Alfred Wegener Institute's Earth system model version 2.5 (AWI-ESM-2.5) with the CryoGridLite permafrost model to investigate the ground thermal regime and freeze-thaw dynamics in northern high-latitude land areas during the MH and the LIG in comparison to the PI. Specifically, we decompose how the annual mean and seasonal amplitude (that is, the difference between the maximum and minimum monthly mean) of surface temperatures affect the occurrence of permafrost, seasonal frost, thaw depth and duration, and thermal contraction cracking activity. For the MH (LIG) AWI-ESM-2.5 simulated global-mean surface temperatures in the simulation domain to be about 0.1 K lower (0.4 K higher), and the global-mean seasonal amplitudes to be 2.9 K (7.4 K) higher than for the PI. With respect to interglacial permafrost characteristics, our simulations revealed that (i) local permafrost probabilities and global permafrost extent are predominantly determined by mean temperatures, (ii) maximum thaw depths are increasing with both annual mean and seasonal amplitudes, and (iii) thermal contraction cracking within the permafrost domain is almost solely driven by the seasonal amplitudes of surface temperatures. Thus, not only mean warming, but also the enhanced seasonal temperature amplitude due to a different orbital forcing have driven permafrost and ground ice dynamics during past interglacial climates. Our results provide an additional explanation of reconstructed periods of marked permafrost degradation in the past, which was driven by deep surficial thaw during summer, while colder winters allowed for permafrost persistence in greater depths. Our results further suggest that past interglacial climates have limited suitability as analogues for future permafrost thaw trajectories, as rising mean temperatures paralleled by decreasing seasonal amplitudes expose the northern permafrost region to magnitudes of thaw that are likely unprecedented since at least Marine Isotope Stage 11c (about 400 ka BP).

# 1 Introduction

During the Quaternary period, Earth's climate underwent substantial climatic fluctuations, marked by alternations of glacials and interglacials over the past several hundred thousand years (Köhler and van de Wal, 2020). These cycles

have profoundly influenced not only the abundance of ice sheets and glaciers, but also the distribution and extent of permafrost in northern mid- and high-latitude land areas (Willeit and Ganopolski, 2015; Lindgren et al., 2018; Saito et al., 2022). During colder climates, organic carbon became freeze-locked within the permafrost deposits, which is hypothesized to have contributed to deglacial warming through the release of greenhouse gases as these permafrost areas thaw (Tesi et al., 2016; Crichton et al., 2016; Jones et al., 2023). Conversely, the retreat of the ice sheets during deglaciations has also facilitated the emergence of new carbon sinks (Lindgren et al., 2018), highlighting the complex interactions between the climate, the cryosphere, terrestrial landscape dynamics, and the carbon cycle (Treat et al., 2019; Brosius et al., 2021; Jones et al., 2023).

Earlier direct and indirect reconstructions of northern hemisphere permafrost extent have suggested markedly smaller permafrost areas during the MH and the LIG compared to the PI (Zoltai, 1995; Anisimov and Nelson, 1996; van Vliet-Lanoë and Lisitsyna, 2001), linking warmer climatic conditions during these periods with substantial permafrost retreat. However, the magnitude, patterns, and dynamics of climatic changes during these interglacial periods remain uncertain to date. On the one hand, proxy records may be biased towards seasons and do not represent mean warming or cooling (Marcott et al., 2013; Bova et al., 2021; Osman et al., 2021; Erb et al., 2022). On the other hand, there are also systematic deviations between model and proxy data, as well as substantial inter-model spreads (Brierley et al., 2020; Otto-Bliesner et al., 2021). For instance, there is no consensus on the magnitude and evolution of global and high-latitude temperatures during the Holocene, with proxy reconstructions pointing to a global mid Holocene thermal optimum warmer than the present, while modelling works suggest a steady global temperature increase throughout the Holocene with only regionally warmer but globally colder mean surface temperatures compared to the PI (Kaufman and Broadman, 2023). This "Holocene temperature conundrum" has been partly attributed to seasonal biases in the proxy records (Bova et al., 2021), and poor spatial averaging of unevenly distributed proxies (Osman et al., 2021). Despite recent progress towards resolving the conundrum through data assimilation approaches (Osman et al., 2021; Erb et al., 2022), the patterns and evolution of Holocene temperatures remain uncertain (Kaufman and Broadman, 2023). Similarly, LIG temperature reconstructions are uncertain with the additional complication that many terrestrial climate proxies in high latitudes have been vanished during the subsequent glacial. However, there is consensus that, as a general feature, both the LIG and MH surface temperatures featured larger seasonal amplitudes in the land areas of the northern hemisphere compared to the PI (O'ishi et al., 2021; Shi et al., 2022; Brierley et al., 2020), mainly as a consequence of the greater obliquity of the Earth's orbit (i.e. the tilt of its rotational axis) (Kwiecien et al., 2022).

Reconstructing ground temperatures and potential permafrost dynamics of the past is challenging. On timescales of decades to multiple centuries, ground surface temperatures of the past can be reconstructed from inverting the temperature profiles obtained from deep boreholes (Pollack and Huang, 2000; Liu et al., 2021), where the latent heat effect due to ground freezing and thawing is adding complexity (Groenke et al., 2023, 2024). On longer, orbital timescales of multi-millennia, the direct observational record is not suited, but proxy records can provide information about the characteristics of permafrost. For example, characteristic landforms like ice-wedge casts and sand forms can be used to infer the presence of permafrost during the past (Christiansen et al., 2016), and have been used to delineate the southern limits of the permafrost region during the last glacial period (Vandenberghe et al., 2014; Lindgren et al., 2018). Conversely, these landforms are not suited to infer the absence of permafrost, such as the limits of the permafrost region during past interglacials. Such reconstructions can be done indirectly, by establishing relations between past vegetation via pollen records and climate conditions (Klemm et al., 2013). However, there are limitations due to sparse spatio-temporal sampling, potential seasonal biases, and interpretative uncertainties. Speleothem growth records from karstic cave systems provide another mean to infer the absence or presence of permafrost in the past (Vaks et al., 2013; Biller-Celander et al., 2021; Yan et al., 2025; Umbo et al., 2025): As a sustained supply water infiltrating the cave is required for the build-up of speleothems, the presence of permafrost above the cave would preclude growth. Hiatuses in a continuous record of dated speleothem layers, are thus a possible indication of permafrost presence, while records of growth suggest permafrost absence. However, speleothem records are spatially constraint to karst regions, and their interpretation can be ambiguous, in particular when in zones of discontinuous permafrost occurrence.

In the absence of highly-suitable proxy records, paleoclimate modelling provides another mean to retrace the characteristics and abundance of permafrost in the past. While much effort in paleoclimate modelling is dedicated to surface temperature reconstructions, only few works specifically addressed model-based reconstructions of permafrost and seasonal frost conditions during past climates (Liu and Jiang, 2016; Saito et al., 2022; Guo et al., 2023). Classical freezing/thawing degree-day models used for approximating permafrost conditions (Riseborough et al., 2008) already suggest that the presence and characteristics of permafrost and seasonally frozen ground are not only controlled by the mean annual temperature at the surface, but also by the seasonal temperature amplitude. For similar annual mean temperatures, marked differences in seasonal amplitude can result in distinct permafrost characteristics including the thickness of the active layer (Riseborough et al., 2008), the duration of thaw, or the occurrence of thermal contraction cracking (Lachenbruch, 1962; Matsuoka et al., 2018). These factors

in turn exert key control on hydrological, geomorphological, and biogeochemical processes (Liljedahl et al., 2016; Walter Anthony et al., 2024; Lyu et al., 2024, e.g.). Thus, the seasonal temperature amplitude emerges as a potentially critical factor when reconstructing the interplay between permafrost and environments, ecosystems, and landscape dynamics during past interglacials.

Here, we assess the effects of the mean and seasonality of surface temperatures on the ground thermal regime in northern mid- and high-latitude land areas during the last and current interglacial. The PI, MH, and LIG climate states are particularly suited for this analysis, on the one hand due to the availability of paleoclimate reconstructions based on proxy records from pollen and speleothems, and on the other hand due to consistent definitions of boundary conditions for simulations in the scope of the Paleoclimate Model Intercomparison Project Phase 4 (PMIP4). Specifically, we address the following objectives:

1. To evaluate the simulated interglacial permafrost extents against proxy-based permafrost reconstructions based on paleo records of speleothem growth and pollen.

2. To quantify ground thermal characteristics including (i) the probability and extent of permafrost, (ii) the maximum annual thaw depths (active-layer thicknesses), and (iii) the thermal contraction cracking activity, in the northern hemisphere (north of 30° N) for different interglacial climates (PI, MH, and LIG).

3. To decompose the contributions of the annual mean and the seasonal amplitude of surface temperatures on these ground thermal characteristics, at the global scale as well as at continental scales (that is, North America, northern Eurasia, and southern Eurasia including the Tibetan plateau).

For this, we diagnose parameter-ensemble simulations of the dedicated permafrost model CryoGridLite (Langer et al., 2024) which are driven by climatic forcing time series of different means and seasonal amplitudes of surface temperatures, generated from the output of the fully coupled Earth system model (ESM) AWI-ESM-2.5 (Shi et al., 2022). To provide a perspective on potential future thaw trajectories, we contextualize our findings for the interglacial climates with model simulations of different future climate scenarios.

## 2 Methods

### 2.1 Simulations of interglacial climates using AWI-ESM-2.5

We used the coupled Earth system model AWI-ESM-2.5 (Sidorenko et al., 2019; Shi et al., 2020, 2022) at an atmosphere resolution of T63 (192 longitudes and 96 latitudes with a resolution of $1.875° \times 1.875°$ near the equator) to simulate equilibrium climates under the boundary conditions of PMIP4 for the PI, MH, and LIG (Otto-Bliesner et al., 2021) (Table 1). The experiments were run with dynamic vegetation, but otherwise identical, static input datasets (e.g., glacier mask, topography, etc.) which are reflective of PI conditions. The PI simulation was run for a total of 3000 years. After 1600 years, the MH and LIG simulations were branched off and integrated for another 1400 years. The establishment of a quasi-equilibrium state was confirmed in all experiments by a diminishing trend in global sea surface temperatures of less than 0.05 K per century (Zhang et al., 2013).

From each experiment, we used the last 100 simulation years to construct a time series of daily mean surface temperatures (variable `tsurf` in ECHAM6, hereafter referred to as $T_a$) and daily snowfall rates (variable `prsn` in ECHAM6) for all 2403 land grid cells northward of 30° N to be used as climatic forcing for the CryoGridLite permafrost model (see Sect. 2.2). Figure 1 provides an overview of the mean and seasonal amplitude of surface temperatures in the simulation domain. The seasonal amplitude was taken as the difference between the highest and lowest monthly mean surface temperature.

In addition, we created six alternative climate forcing time series in which we combined the mean temperature and the seasonal temperature amplitude of the original PI, MH, and LIG experiments. For each original experiment (PI, MH, and LIG) we applied the temperature anomalies with respect to each of the other two experiments to the entire time series of daily mean surface temperatures ($T_a(x, y, t)$), that is, for each grid point $(x, y)$:

$$T_a^{\overline{\alpha}\tilde{\beta}}(x, y, t) = T_a^{\overline{\beta}\tilde{\beta}}(x, y, t)$$
$$+ \left( \left\langle T_a^{\overline{\alpha}\tilde{\alpha}} \right\rangle_t (x, y) - \left\langle T_a^{\overline{\beta}\tilde{\beta}} \right\rangle_t (x, y) \right) \quad (1)$$

where $\alpha, \beta \in \{PI, MH, LIG\}$, $\bar{\cdot}$ denotes the annual mean, $\tilde{\cdot}$ the seasonal amplitude, and $\langle \cdot \rangle_t$ denotes the temporal mean over the entire forcing time series. In doing so, the seasonal amplitudes of the original forcing were retained, while the mean temperatures were adjusted to those of the other climate states. The snowfall time series were left unchanged and therefore correspond to those of the climate characterizing the seasonal amplitude. In total, we obtained nine climate forcing time series corresponding to all combinations of the means and seasonal amplitudes of the PI, MH, and LIG surface temperatures.

### 2.2 Ensemble-simulations of ground thermal regimes using CryoGridLite

#### 2.2.1 Model description and input data

We used the climate forcing time series generated from the AWI-ESM-2.5 output to drive dedicated simulations with the CryoGridLite permafrost model (Nitzbon et al., 2023; Langer et al., 2024). CryoGridLite simulates subsurface heat

**Table 1.** Greenhouse gas concentrations and orbital parameters used as boundary conditions for the AWI-ESM-2.5 experiments, following the PMIP4 protocol (Otto-Bliesner et al., 2017). Global-mean surface temperature ($\overline{T}_a^{\text{global}}$) and global-mean surface temperature seasonality ($\tilde{T}_a^{\text{global}}$) are shown as well.

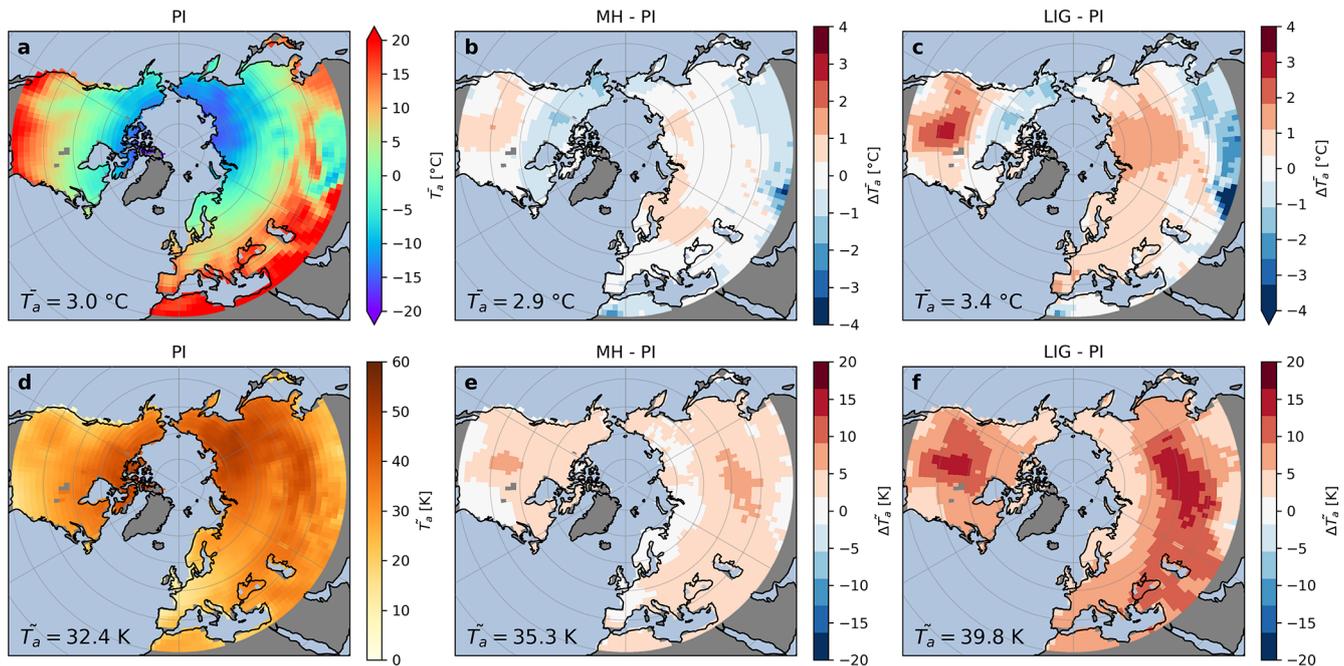| | Greenhouse gas concentrations | | | Orbital parameters | | | Climate characteristics | |
|---|---|---|---|---|---|---|---|---|
| Experiment | $CO_2$ (ppm) | $CH_4$ (ppb) | $N_2O$ (ppb) | Eccentricity | Obliquity (°) | Perihelion (°) | $\overline{T}_a^{\text{global}}$ (°C) | $\tilde{T}_a^{\text{global}}$ (K) |
| PI | 284.3 | 808.2 | 273.0 | 0.016764 | 23.4598 | 100.338 | 14.21 | 11.4 |
| MH | 264.4 | 597.0 | 262.0 | 0.018682 | 24.1058 | 0.878 | 13.88 | 12.1 |
| LIG | 275.0 | 685.0 | 255.0 | 0.039378 | 24.0408 | 275.418 | 14.06 | 12.7 |



**Figure 1.** Overview of the mean ($\overline{T}_a$) and seasonal amplitude ($\tilde{T}_a$) of surface temperatures in the simulation domain simulated by AWI-ESM-2.5. Absolute values are shown for the pre-industrial (PI; (**a**), (**d**)), and anomalies (indicated as $\Delta\overline{T}_a$ and $\Delta\tilde{T}_a$) relative to the PI are shown for the Mid Holocene (MH; (**b**), (**e**)) and the Last Interglaical (LIG; (**c**), (**f**)).

conduction under consideration of the phase change of water using daily-mean surface temperatures as an upper boundary condition. As the lower boundary condition, a constant geothermal heat flux is prescribed at a depth of $z = 500$ m (Langer et al., 2024). The model further simulates the dynamic build-up, compaction, and ablation of a snowpack using daily snowfall rates as input. While the version of CryoGridLite used for this study does not simulate the surface and subsurface hydrology dynamically, it addresses the spatial variability of subsurface water/ice contents through parameter-ensemble simulations.

We created an ensemble of size $n_{\text{ens}} = 100$ of parameters and ground stratigraphies reflecting subgrid-scale variability of surface and subsurface environmental conditions. Following Nitzbon et al. (2023) and Langer et al. (2024), the ground stratigraphy was varied within the ensemble by uniformly sampling the water/ice contents in (i) the root

zone between the wilting point and the field capacity ($\theta_R \in [\theta_{\text{wp}}, \theta_{\text{fc}}]$), (ii) the vadose zone between the field capacity and the porosity ($\theta_V \in [\theta_{\text{fc}}, \phi]$), and (iii) the bedrock zone, where the water/ice content was reduced to a value $\theta_B \in [0, \phi]$ while increasing the mineral content to retain saturated conditions. To represent the spatial variability of ground surface temperatures, we randomly drew from a uniform distribution (i) a maximum snow height $h_{\text{snow,max}} \in [0.1, 2.0]$ m, (ii) a snowfall multiplier $f_{\text{sn}} \in [0.5, 1.5]$, and (iii) a thawing-season temperature scaling factor $n_t \in [0.5, 1.0]$ (Kropp et al., 2020).

Compared to the CryoGridLite simulations in Nitzbon et al. (2023) and Langer et al. (2024), we extended the simulation domain from the contemporary permafrost region to the land area northward of 30° N. For the contemporary permafrost domain, we obtained soil organic carbon contents from the dataset by Hugelius et al. (2014), which repre-
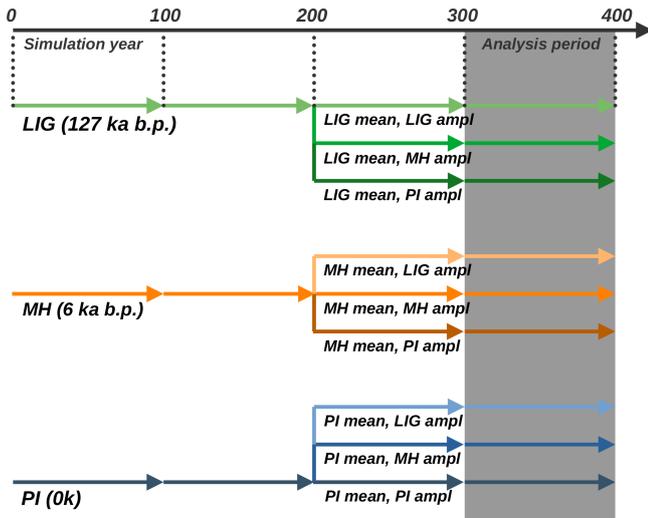
**Figure 2.** Overview of the simulation protocol. After a 200-year spin-up of each original climate forcing (PI, MH, LIG), three experiments, in which the climate forcing had the same mean temperatures, but different seasonal amplitudes were branched off and continued for another 200 years. The final 100-year period was used for the analyses.

sents the upper 3.0 m of the subsurface. Outside the contemporary permafrost region, we used the dataset by FAO and ITPS (2018) which only represents carbon stocks in the upper 0.3 m of the subsurface. Otherwise, we used the same input datasets as described in Langer et al. (2024) which have global coverage. All input datasets were regridded to a Cartesian grid with a spatial resolution of $1.875° \times 1.875°$.

### 2.2.2 Experiments

We performed nine model experiments which used identical ensembles of ground stratigraphies and parameters, but different forcing time series representing all combinations of means and seasonal amplitudes of surface temperatures in the PI, MH, and LIG as described above (Fig. 2). The ground temperatures of each simulation were initialized based on an equilibrium temperature profile. First, we ran a 200-year simulation for the PI, MH, and LIG by repeating each of the original forcing time series twice. Each of these simulations was then continued for another 200 years by repeating the original forcing time series twice. In addition, we branched off two further 200-year simulations, in which we repeated the alternative forcing time series of the same mean but different amplitudes twice. The first 300 years of each experiment were considered as spin-up to obtain a dynamic equilibrium of the ground thermal regime within at least the upper $\approx 10$ m of the subsurface. The final 100 years of each experiment were used for further analysis.

### 2.2.3 Diagnostics

We diagnosed different characteristics of the ground thermal regime which are of relevance to various processes and feedbacks acting in periglacial landscapes. First, we diagnosed the occurrence of permafrost as follows:

– We determined the *permafrost probability* ($p_{PF}$) as the fraction of ensemble members for which the maximum annual temperature in 10 m depths (averaged over the 100-year analysis period) is below $0°C$. Assuming the ensemble is representative of the actual spatial variability of environmental conditions, the permafrost probability corresponds to the areal fraction of the landscape underlain by permafrost, and the overall permafrost area ($\Omega_{PF}$) was obtained as $\Omega_{PF} = \sum_{x,y} p_{PF}(x,y)\omega(x,y)$ where $\omega(x,y)$ is the land area of grid cell $(x,y)$. The permafrost probability is a general indicator for the absence or presence of permafrost with implications for all landscape and ecosystem functions affected by permafrost, including hydrology, biogeochemistry, and geomorphology.

Based on the permafrost probabilities, we defined the joint permafrost domain as all grid cells for which $p_{PF} > 0$ in any of the nine simulations. For the joint permafrost domain, we further diagnosed the following quantities:

– The *maximum annual thaw depth* ($d_{thaw}^{max}$ (m)) was determined as the annual maximum of the depth-integrated thawed ground fraction within the upper 3 m of the subsurface (averaged over the 100-year analysis period). Thus, it is limited to a maximum of 3 m. For thaw-depths beyond 3 m, the ground can be considered to be permafrost-free. If not stated otherwise, the ensemble-mean of the maximum annual thaw depth is provided. The maximum annual thaw depth corresponds to the depth of the active layer in permafrost areas, and has important implications for hydrology and biogeochemistry. Moreover, deeper thaw makes the initiation of thermokarst and other rapid thaw processes in ice-rich terrain more likely and can thus trigger substantial geomorphological changes.

– Similar to Stadelmaier et al. (2021), we adopted the thresholds for thermal contraction cracking provided in Matsuoka et al. (2018) to diagnose the *(deep) thermal contraction cracking activity* ($a_{FC}^{deep}$ (d yr$^{-1}$)) as the number of days per year for which the ground temperature in 1 m depth is $T_{1m} < -10°C$, and the temperature gradient in the upper meter of the subsurface is $\nabla T_{1m} > 10°C\,m^{-1}$, implying a ground surface temperature of $T_{0m} < T_{1m} - 10°C$. We always report the mean over the analysis period and the ensemble. The thermal contraction cracking activity is a first order estimate for the possibility of wedge-ice formation. In these areas, excess ice growth is more likely, which can have

a stabilizing effect on shorter timescales (Kanevskiy et al., 2017), but might make the landscape vulnerable to thermokarst on longer timescales.

We further diagnosed the seasonal frost probability ($p_{SF}$), the annual thawed ground fraction within the upper 3 m of the subsurface ($D_{thaw}^{3\,m}$), and the shallow thermal contraction cracking activity ($a_{FC,shallow}$) within the joint seasonal frost domain as described in Appendix A.

## 2.3   Model evaluation against paleo records

To assess whether our model setup is capable of reproducing past interglacial permafrost extents realistically, we compared the simulated permafrost probabilities of the MH and LIG experiments to different paleo records.

### 2.3.1   Speleothem growth

First, we considered speleothem growth records, which are suitable for comparisons on glacial-interglacial time scales due to their high resistance to surface erosion (Kwiecien et al., 2022). Growth periods in the speleothem layering can be used as an indicator for absence of permafrost, while hiatuses can suggest permafrost presence, as it precludes deep ground water infiltration and thus inhibits speleothem growth. However, other factors can cause hiatuses or markedly modify speleothem growth as well, such as arid climates (Geyh and Heine, 2014; Nicholson et al., 2020), flooding of the cave (Denniston and Luetscher, 2017; González-Lemos et al., 2015), or glaciers (Spötl et al., 2024). For this study, we compiled speleothem growth data from different sources (Müller-Ißberner et al., 2024), including mainly the SISALv3 database (Kaushal et al., 2024) and additional data points from individual studies (Biller-Celander et al., 2021; Batchelor et al., 2019; Vaks et al., 2013; Lauritzen, 1995; Lauritzen and Lundberg, 1999; Dublyansky et al., 2018; Žák et al., 2012; Batchelor et al., 2024). For the MH (LIG), we used all available data northward of 20° N with growth periods and hiatuses with durations longer than 500 years dated between 5 (126) and 6 (127) ka BP, obtaining a total of $n = 93$ ($n = 47$) individual locations with one or more speleothem records. We considered locations with speleothem hiatuses to be in agreement with the model if the simulated permafrost probability was $p_{PF} > 10\%$, and locations with speleothem growth to be in agreement with the model if $p_{PF} < 90\%$. Therefore, in regions where the simulated permafrost coverage was sporadic or discontinuous ($10\% < p_{PF} < 90\%$), both speleothem growth and hiatuses were considered plausible.

### 2.3.2   Pollen

We additionally considered the Holocene permafrost reconstruction by Li et al. (2022), who compiled a multitude of

modern and fossil pollen records from Eurasia to establish a logistic regression model predicting permafrost coverage (classified as "permafrost-free", "non-continuous permafrost", or "continuous permafrost") based on the abundance of different pollen. Simulated permafrost probabilities of $p_{PF} \leq 10\%$ were considered to agree with the reconstruction if the pollen record indicated "permafrost-free" conditions. Probabilities of $p_{PF} \geq 90\%$ were associated with "continuous permafrost", and $10\% < p_{PF} < 90\%$ with "non-continuous" permafrost.

## 3   Results

### 3.1   Comparison between simulated and proxy-based interglacial permafrost extents

#### 3.1.1   Speleothem growth

For both the MH and LIG, there is only one location out of 83 (33), the Tianmen cave on the southern Tibetan plateau, which is showing speleothem growth during the MH (Cai et al., 2012) and LIG (Cai et al., 2010), while our simulations suggest a high permafrost probability $> 90\%$ (Fig. 3a, d). In addition, one location, located in the Nahanni plateau region of northwest Canada (Biller-Celander et al., 2021; Batchelor et al., 2024), shows both speleothems with growth and with hiatuses during the LIG, while our simulations suggest a high permafrost probability (Fig. 3e). All other records of speleothem growth are plausibly located outside the region where the simulated permafrost probabilities are $> 90\%$.

Vice versa, almost all speleothem hiatuses in the latitudes northward of 50° N are consistently located within the region where the simulated permafrost probabilities are $> 10\%$. One exception is a record in northern Scandinavia during the LIG, which is close to the simulated permafrost region. This deviation could be explained by subglacial flooding of the cave galleries during the penultimate deglaciation (Lauritzen, 1995). Several hiatuses in lower latitudes (southward of 50° N) are located far outside the simulated permafrost region. These can likely be attributed to either other origins like aridity, flooding, ice sheet remnants, or mountain permafrost settings that are not resolved in our model. Overall, the southern limit of the Arctic permafrost region simulated with AWI-ESM-2.5/CryoGridLite is broadly consistent with the speleothem records. However, due to its relatively sparse spatial coverage, the speleothem record does not provide a tight constraint on the past interglacial permafrost extents.

#### 3.1.2   Pollen

We used the pollen-based reconstruction of Li et al. (2022) for northern Euraisa during the MH to partly compensate for the sparse spatial coverage of speleothem records. For the "continuous permafrost" category, 58 out of 72 records are located within the region where simulated permafrost probabilities are $> 90\%$ (Fig. 3a, c). Most of the 14 misaligned
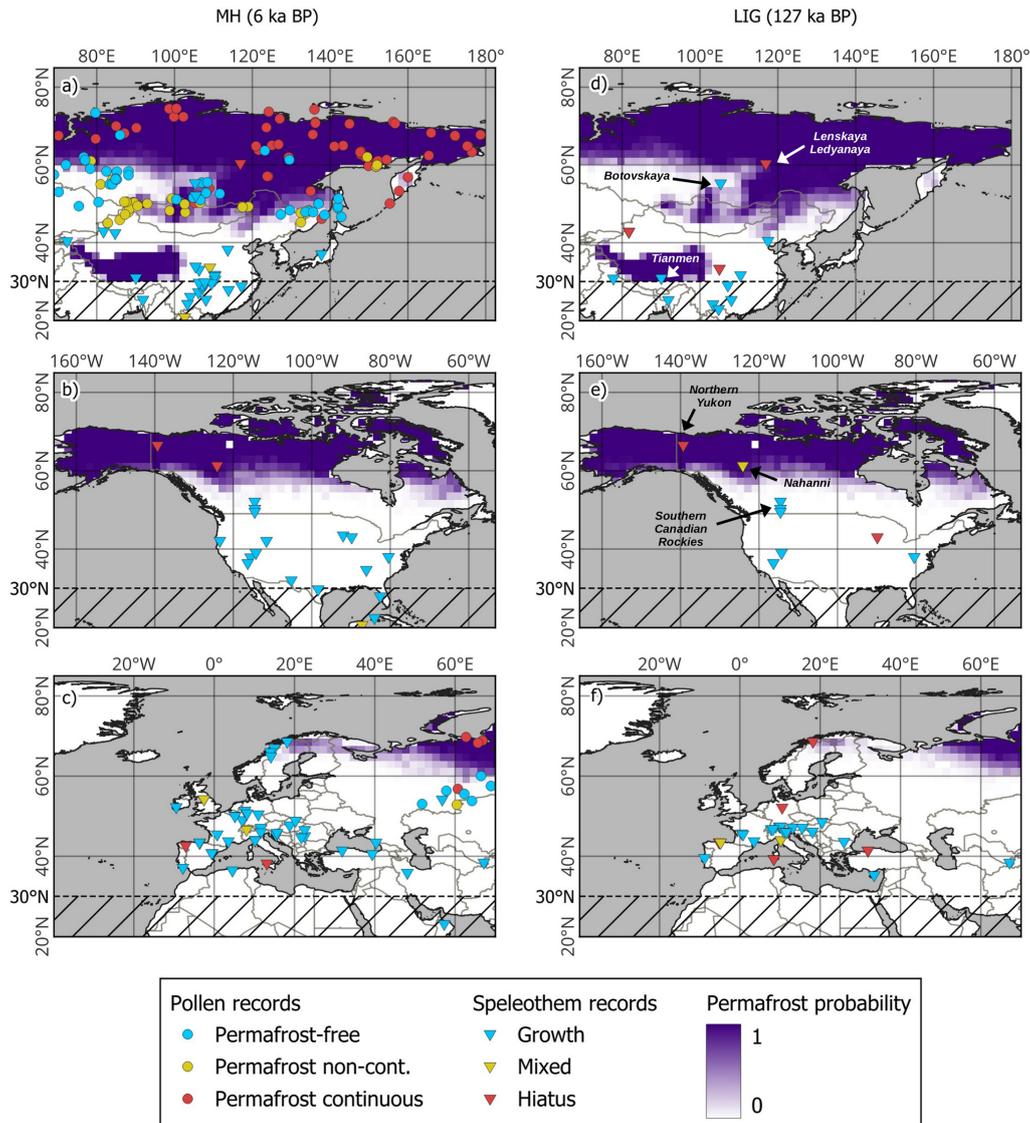
**Figure 3.** Simulated permafrost probabilities for the MH (**a, b, c**) and LIG (**d, e, f**) together with permafrost proxies based on speleothem growth (diamond marker) and pollen records (circles). Speleothem growth indicates permafrost absence while hiatuses can be explained by permafrost presence. The mixed category represents locations with records of both speleothem growth and hiatuses during the respective period. Prominent cave systems in the permafrost regions of eastern Eurasia and North America are labelled in panels (**d**) and (**e**). The dotted line at 30° N represents the southern limit of the simulation domain. Note that the pollen records only cover northern Eurasia during the MH.

records are located in eastern and southern Siberia, mostly within regions with simulated non-continuous permafrost. For the "permafrost-free" category, 20 out of 46 records are located within the regions where permafrost probabilities are $< 10\%$, with most of the unaligned records located within the transitional area where simulated permafrost is non-continuous. This could indicate a slight southward overestimation of the simulated Eurasian permafrost extent. For the "non-continuous" permafrost category the agreement is the lowest, with only 10 out of 33 records within areas with a permafrost probability between 10 % and 90 %. However, most of the non-continuous permafrost records are clus-

tered in the central Asian region between Kazakhstan, Russia, China and Mongolia, for which the model mostly simulates permafrost-free conditions. This could partly be related to high-altitude settings not resolved in the model. As there are few pollen records suggesting non-continuous permafrost in western and eastern Siberia, the pollen-based regression model for "non-continuous" permafrost does not provide a conclusive constraint on the southern permafrost limit. Overall, the pollen-based permafrost reconstruction agrees relatively well with the simulated permafrost probabilities, even though the "permafrost-free" records might suggest a slight

southward overestimation of the Eurasian permafrost extent in our model.

## 3.2 Simulated interglaical ground thermal characteristics

### 3.2.1 Permafrost and seasonal frost probability and extent

For the PI, we simulated a northern hemisphere permafrost area of $18.8 \times 10^6$ km$^2$ (Fig. 4a). For the MH, the simulated permafrost area ($19.4 \times 10^6$ km$^2$) is higher than for the PI, with the permafrost area extending further southward in its central part of North America and in eastern Siberia, as well as in parts of the Tibetan plateau, while it is slightly smaller in western Siberia and northern Fennoscandia (Fig. 4e). For the LIG, the simulated permafrost area of $17.8 \times 10^6$ km$^2$ is smaller than those simulated for the PI and MH, mainly due to a reduced extent in western and central Siberia and northern Fennoscandia, while the southernmost parts of Eurasia show higher permafrost probabilities with similar patterns as for the MH (Fig. 4i). On the North American continent, the difference in permafrost areas between the LIG and the PI is modest, with some regions showing more, and some less permafrost.

Considering the alternative climate forcings, we found almost identical patterns of permafrost probabilities for those climate forcings which have the same mean temperatures, that is, for each of the columns in Fig. 4. At the same time the patterns of permafrost probabilities for identical seasonal amplitudes differ in the same way as those of the original (unbiased) forcings (each row in Fig. 4). These patterns suggest, that the (local) permafrost probability is primarily affected by the mean surface temperature, while the seasonal amplitude has only a modest influence.

The primary influence of mean temperature on permafrost presence was also indicated by high negative correlations between the mean temperatures and permafrost area at the global scale and at continental scales (Fig. 5e–h). Across all nine simulations, the permafrost extent and mean temperature showed statistically significant correlations at the hemispheric scale ($r = -0.97$), as well as for northern Eurasia ($r = -0.97$), the Tibetan plateau ($r = -0.95$), and the North American permafrost region ($r = -0.87$). The respective correlations between permafrost extent and seasonal temperature amplitude are all negative, but statistically not significant and fairly low (northern hemisphere: $r = -0.21$; northern Eurasia $r = -0.06$; Tibetan plateau: $r = -0.05$), with the exception of North America ($r = -0.46$, Fig. 5h), where the simulated permafrost extent tended to be lower in climates with a higher seasonal amplitude.

For seasonal frost area (including permafrost), we found a negative but statistically not significant correlations with mean temperatures (northern hemisphere: $r = -0.45$), but significant positive correlations with seasonal amplitude (northern hemisphere: $r = 0.88$) (Fig. 5m). Similar correlations were found regionally (Fig. 5n–p). As visible from Fig. A1, higher seasonal amplitudes of the MH and LIG increase the seasonal frost probability outside the permafrost domain, while the higher mean temperatures of the LIG cause a reduction of $p_{SF}$. These opposing effects are partly compensating each other in the original MH and LIG climates (Fig. A1e, i).

### 3.2.2 Maximum thaw depth and thawed ground fraction

The results for the maximum annual thaw depth (i.e., the active layer thickness in permafrost areas) reveal more complex patterns and dependencies on mean temperatures and seasonal temperature amplitudes than those for the permafrost probabilities (Fig. 6). The average maximum thaw depth across the joint permafrost region was 1.61 m in the PI and thus lower than in the MH (1.64 m) and LIG (1.80 m).

For the MH, maximum thaw depths are larger (deeper active layers) compared to the PI across northern Eurasia and particularly in northern Fennoscandia and western Siberia, while they are smaller (shallower active layers) in more southern latitudes including south-eastern Siberia and the Tibetan plateau (Fig. 6e). In North America, the MH-PI thaw-depth anomalies are modest. For the LIG, we simulated substantially larger thaw depths across the high-latitude permafrost region, with marked increases along its southern margin in Eurasia, coinciding with the regions where permafrost extent is smaller (Fig. 4i). Only for parts of the Tibetan plateau and south-eastern Siberia, the thaw depths are shallower in the LIG climate compared to the PI reference.

For the alternative climate forcings, we found different regional patterns. On the North American continent, thaw depths are substantially increasing for the higher seasonal amplitudes of the MH and LIG climates when the mean temperatures are fixed at PI levels (Fig. 6d, g). When the PI seasonal temperature amplitude was fixed and the mean temperatures shifted, thaw depths were substantially smaller for both the MH and LIG mean temperatures (Fig. 6b, c), consistent with the PI climate being the warmest simulated for the North American permafrost region. These opposing trends for the North American continent more or less cancel each other out in the other simulations (Fig. 6e, f, h), with only the original LIG climate showing substantially deeper thaw than the PI. In northern Eurasia, both the mean and the amplitude are increasing from PI over MH to LIG climate, resulting in substantially deeper thaw depths than for the PI in this region in all simulations. In southern Eurasia including the Tibetan plateau, deeper thaw depths are associated with the higher seasonal amplitudes of the MH and LIG climates (Fig. 6d, g), while shallower thaw depths were simulated for the MH and LIG mean temperatures, as these are colder in this region (Fig. 6b, c). Similar to the pattern found for North America, these effects are partly cancelling each other out in the remaining simulations (Fig. 6e, f, h, i).
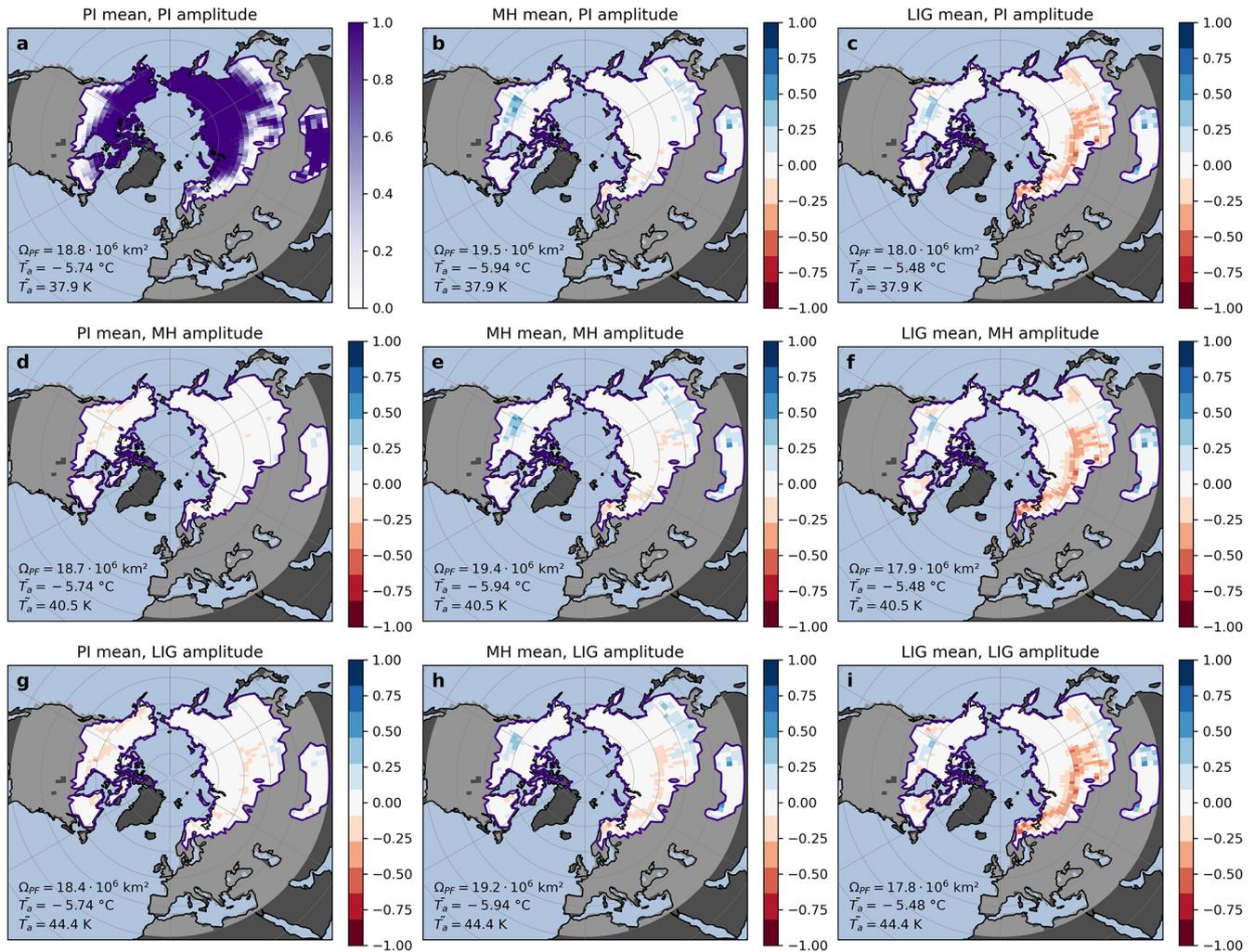
**Figure 4.** Simulated permafrost probabilities ($p_{PF}$) for all climate forcings, shown as absolute values for the pre-industrial (PI) experiment (**a**), and as anomalies relative to the PI for all other experiments (**b–i**). The results for the original climate forcings are shown on the on the diagonal (PI: (**a**); MH: (**e**); LIG: (**i**)), and the off-diagonal panels show results for the alternative climate forcings, with each column having the same mean temperature (PI: (**a**), (**d**), (**g**); MH: (**b**), (**e**), (**h**); LIG: (**c**), (**f**), (**i**)) and each row having the same seasonal temperature amplitudes (PI: (**a**), (**b**), (**c**); MH: (**d**), (**e**), (**f**); LIG: (**g**), (**h**), (**i**)). The purple line marks the limits of the joint permafrost domain of all simulations. The permafrost area ($\Omega_{pf}$), the mean annual temperature ($\overline{T_a}$), and the mean seasonal temperature amplitude ($\tilde{T}_a$) for the joint permafrost domain are given in the lower left corner of each panel.

For the northern hemisphere joint permafrost region (Fig. 5a) the maximum thaw depth showed a positive correlation with both the mean ($r = +0.46$) and the seasonal amplitude ($r = +0.89$) of the surface temperatures, but only the latter is statistically significant (Fig. 5e). Similar correlation values were found for the North American permafrost region ($r = +0.56$ for the mean; $r = +0.82$ for the amplitude; Fig. 5h). On the Eurasian continent, the maximum thaw depth showed a stronger and significant positive correlation with mean temperatures (Eurasia: $r = +0.73$; Tibetan plateau: $r = +0.80$), while the correlations with temperature amplitude were smaller (Eurasia: $r = +0.68$; Tibetan plateau: $r = +0.59$; Fig. 5f, g).

As the maximum thaw depth only captures the deepest extent of thaw but not its duration, we conducted the same analysis also for the annual thawed ground fraction ($D_{thaw}^{3\,m}$) as defined in Appendix A (Fig. A2). In contrast to the maximum thaw depth, the annual thawed ground fraction is primarily affected by the annual mean temperature (northern hemisphere: $r = 0.98$), while the seasonal temperature amplitude showed a minor negative, insignificant correlation ($r = 0.09$; Fig. 5m). Similar correlation scores were found for northern and southern Eurasia (Fig. 5n, o), while for North America, also the seasonal amplitude showed a positive but statistically not significant correlation with thawed ground fraction ($r = 0.46$, Fig. 5p).
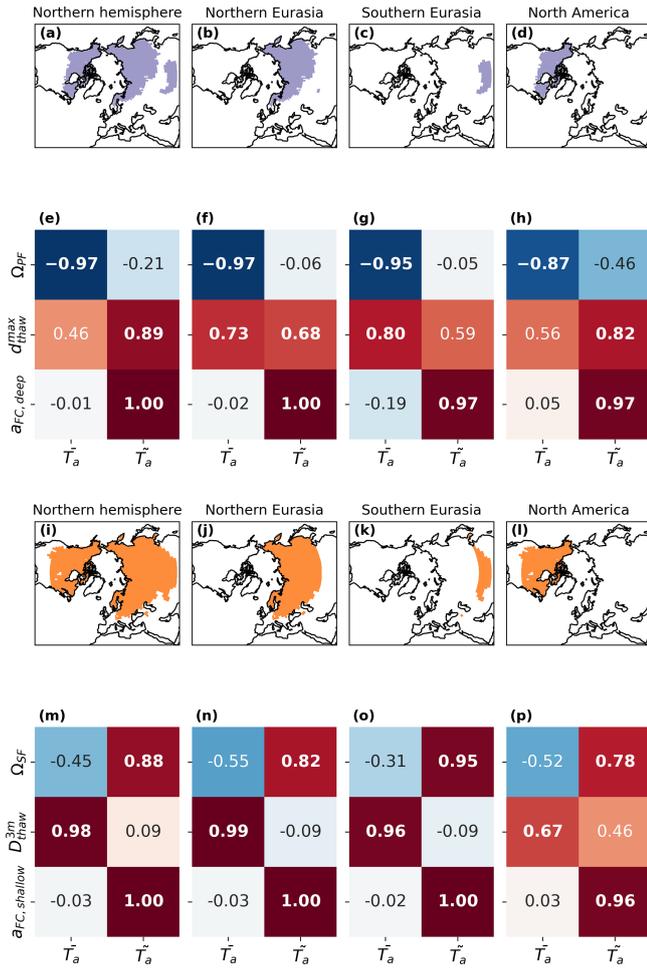
**Figure 5.** Northern hemisphere and regional Pearson correlations between different diagnostics and the mean temperatures ($\overline{T_a}$) and the seasonal temperature amplitudes ($\tilde{T}_a$) of all nine experiments. Statistically significant ($p < 0.05$) correlations are shown in bold font. Panels **(a)**–**(d)** and **(i)**–**(l)** respectively show the part of the joint permafrost and seasonal frost domains which are considered for the correlation analysis in the panels below (northern hemisphere: lat $> 30°$ N; northern Eurasia: lat $> 40°$ N, $0°$ E $<$ lon $< 186°$ E; southern Eurasia: lat $< 40°$ N, $0°$ E $<$ lon $< 186°$ E; North America: lat $> 30°$ N, $186°$ E $<$ lon $< 360°$ E). For the joint permafrost domain **(e–h)**, we considered the permafrost area ($\Omega_{PF}$), the maximum thaw depth ($d_{thaw}^{max}$), and the deep thermal contraction cracking activity ($a_{FC,deep}$). For the joint seasonal frost domain **(m–p)**, we considered the seasonal frost area ($\Omega_{SF}$), the thawed ground fraction ($D_{thaw}^{3\,m}$), and the shallow thermal contraction cracking activity ($a_{FC,shallow}$).

### 3.2.3  Thermal contraction cracking activity

In all simulations, deep thermal contraction cracking was most probable in the continental parts of Eurasia including northern and southern central Siberia (Fig. 7). The overall deep thermal contraction cracking activity was lowest in the PI simulation ($\overline{a_{FC,deep}} = 0.34$), substantially higher for the

MH ($\overline{a_{FC,deep}} = 0.45$), and almost twice as high for the LIG ($\overline{a_{FC,deep}} = 0.61$).

For each original climate forcing, changes of the mean temperatures towards those of the other climates did not result in any significant changes in deep thermal contraction cracking patterns and magnitudes (that is, there are identical patterns for each row in Fig. 7). Vice versa, irrespective of the mean temperatures, the deep thermal contraction cracking activity increased with the higher amplitudes of the MH and LIG climates (cf. each column in Fig. 7), overall suggesting a predominant influence of temperature seasonality on deep thermal contraction cracking activity.

The correlation analysis confirms, that at the hemispheric scale, deep thermal contraction cracking activity is not correlated with mean temperatures ($r = -0.01$), but very strongly positively correlated with the seasonal amplitude ($r = +1.00$) (Fig. 5e). Similar correlations were obtained for northern Eurasia (mean: $r = -0.02$, amplitude: $r = +1.00$; Fig. 5f) and North America (mean: $r = 0.05$, amplitude: $r = +0.97$; Fig. 5h). For southern Eurasia, the correlation with the seasonal temperature amplitude was also very strong ($r = +0.97$), but there was also a slightly negative correlation with the mean temperatures ($r = -0.19$; Fig. 5g), suggesting that deep thermal contraction cracking becomes less probable in regions of generally warm permafrost.

Complementary results for the activity of shallow thermal contraction cracking in the joint seasonal frost domain are provided in Fig. A3. Similar to $a_{FC,deep}$, $a_{FC,shallow}$ is almost exclusively driven by the seasonal amplitude (northern hemisphere: $r = +1.00$; Fig. 5m), while the annual mean temperature showed no significant correlations with shallow frost cracking activity both across the northern hemisphere as well as regionally (Fig. 5n–p).

## 4  Discussion

### 4.1  Model accuracy, uncertainties, and limitations

To assess the accuracy and to identify uncertainties and limitations of our model simulations, it is instructive to compare our modelling results to contemporary observations, proxy-based reconstructions and other model simulations of permafrost characteristics.

For the PI, we simulated a northern hemisphere permafrost area of $18.8 \times 10^6$ km$^2$ which exceeds the estimates of Zhang et al. (2000) (($12.2$–$17.0$) $\times 10^6$ km$^2$; late 20th century), Gruber (2012) (($13$–$18$) $\times 10^6$ km$^2$; 1961–1990), and Obu et al. (2019) ($13.9 \times 10^6$ km$^2$; 2000–2016) for recent historical conditions. This can partly be attributed to the PI being colder than the recent historical conditions, but also points to a slight tendency of our AWI-ESM-2.5/CryoGridLite setup to overestimate permafrost probabilities. This can be partly explained by a general cold-bias in the near-surface air temperatures in northern high-latitudes simulated by AWI-ESM-2.5, which could be related to overly simplified soil physics
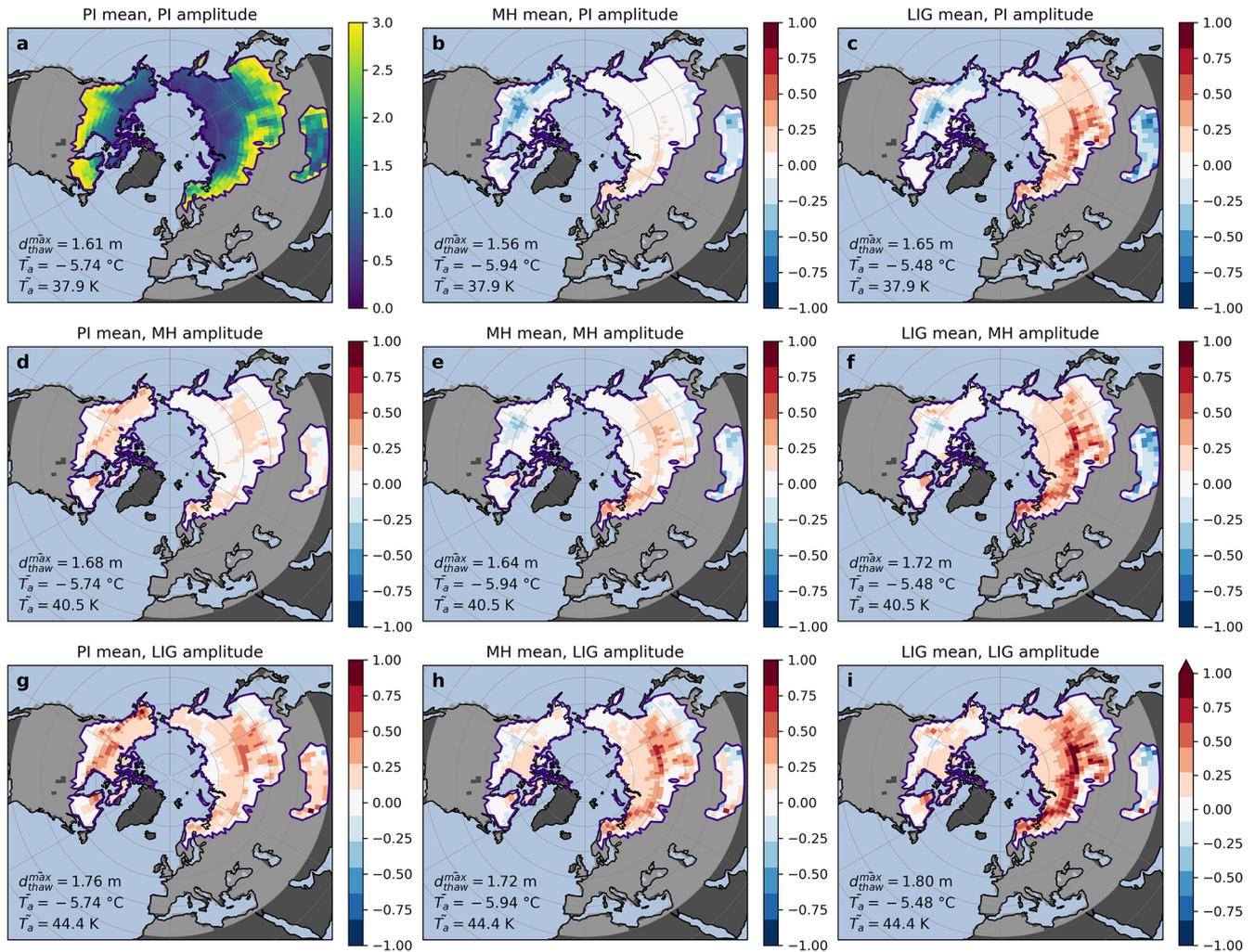
**Figure 6.** Same as Fig. 4, but for the simulated maximum thaw depths ($d_{\text{thaw}}^{\text{max}}$) for all climate forcings, shown as absolute values for the preindustrial (PI) experiment **(a)**, and as anomalies relative to the PI for all other experiments **(b–i)**. The mean maximum thaw depth ($\overline{d_{\text{thaw}}^{\text{max}}}$), the mean annual temperature ($\overline{T_a}$), and the mean seasonal temperature amplitude ($\tilde{T}_a$) for the joint permafrost domain are given in the lower left corner of each panel.

in its land surface scheme JSBACH-3.2 which ignores the phase change of soil water in its default setup.

The higher permafrost area we simulated the MH ($19.4 \times 10^6$ km$^2$) compared to the PI is in contrast to most earlier proxy-based reconstructions and modelling. Early modelling work by Anisimov and Nelson (1996) suggested substantial northward permafrost retreat during the MH (44 % reduction of permafrost region). However, the authors assumed a mean global surface warming of $+1$ °C above modern conditions for the MH climate, which is exceeding more recent estimates for the MH-PI global temperature anomaly (reviewed by Kaufman and Broadman (2023): $+0.54$ K (Marcott et al., 2013); $+0.47$ K (Temp12k, multi-proxy; Kaufman et al. (2020)); $+0.3$ K (LegacyClimate; pollen only; northern hemisphere north of 30° N; Herzschuh et al. (2023)); $+0.12$ K (Holocene DA; data assimilation; Erb et al. (2022));

$-0.15$ °C (LGMR; data assimilation; Osman et al. (2021)); $-0.3$ K (PMIP4-CMIP6 multimodel mean; Brierley et al. (2020))). The MH-PI global temperature anomaly in our AWI-ESM-2.5 experiments amounts to $-0.33$ K and compares well to the lower end of these more recent estimates (Table 1). Similarly, the earlier proxy-based reconstructions by Zoltai (1995) and van Vliet-Lanoë and Lisitsyna (2001) suggested marked MH permafrost retreat. However, these were mostly based on vegetation-derived proxies, which can be biased towards the growing season (Bova et al., 2021; Kaufman and Broadman, 2023) and therefore overestimate warming and the associated permafrost retreat due to the higher temperature seasonality during the MH. Also the pollen-based reconstructions by Li et al. (2022) suggest a more northern permafrost limit during the MH in eastern Eurasia (Fig. 3a), as reconstructions of permafrost-free con-
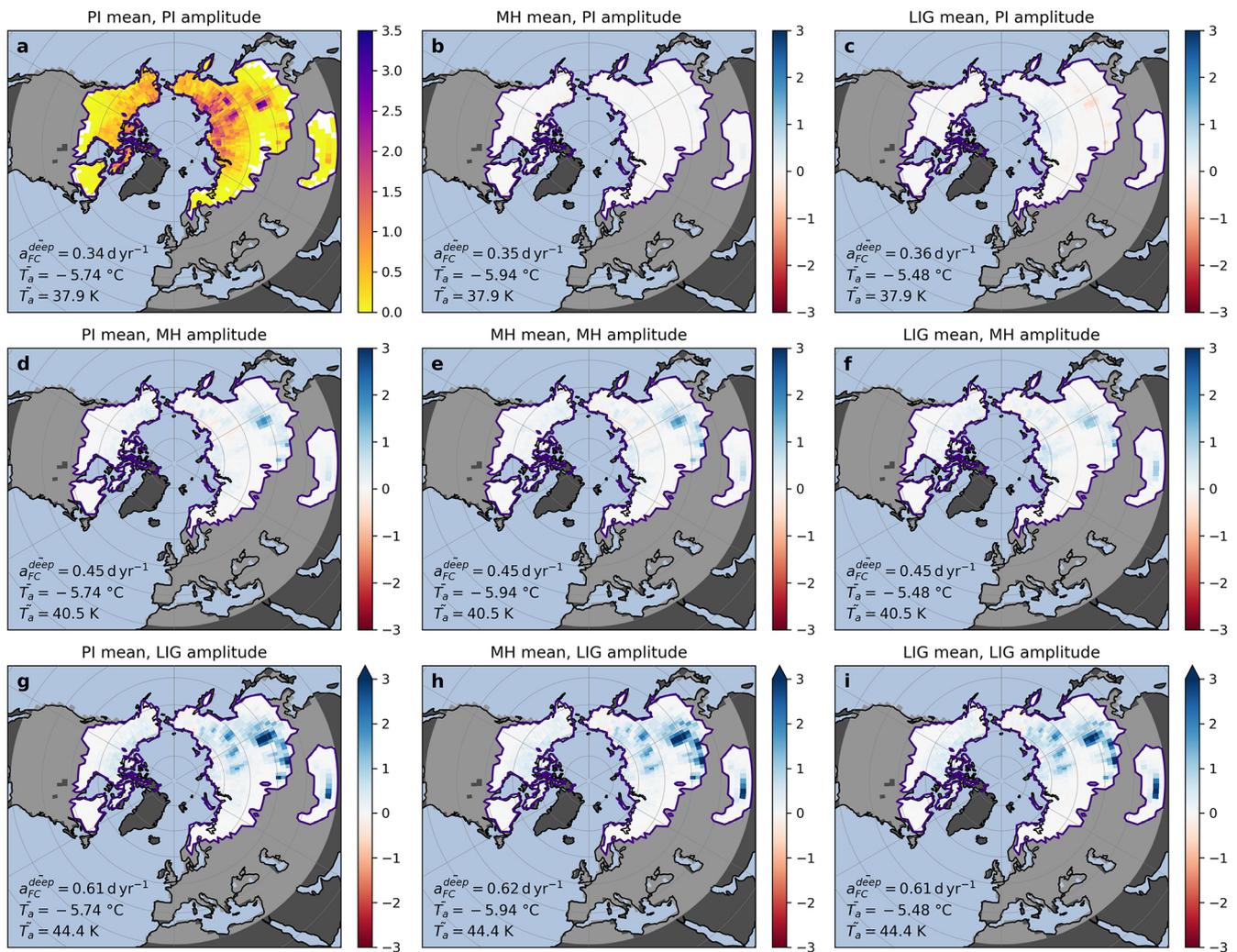
**Figure 7.** Same as Fig. 4, but for the simulated deep thermal contraction cracking activity ($a_{\mathrm{FC}}^{\mathrm{deep}}$; see Sect. 2.2.3 for the definition) for all climate forcings, shown as absolute values for the pre-industrial (PI) experiment **(a)**, and as anomalies relative to the PI for all other experiments **(b–i)**. The mean deep thermal contraction cracking activity ($\overline{a_{\mathrm{FC}}^{\mathrm{deep}}}$), the mean annual temperature ($\overline{T_{\mathrm{a}}}$), and the mean seasonal temperature amplitude ($\tilde{T}_{\mathrm{a}}$) for the joint permafrost domain are given in the lower left corner of each panel.

ditions are located within our simulated discontinuous permafrost zone. However, the pollen-based reconstructions of non-continuous permafrost by Li et al. (2022) do not provide a strong constraint in Siberia, as the corresponding locations are relatively clustered across Mongolia and northwestern China, potentially in mountainous settings, where our model partly simulates permafrost absence. Compared to the reconstructions by van Vliet-Lanoë and Lisitsyna (2001), the work by Li et al. (2022) suggests a less pronounced permafrost retreat during the MH, and is thus closer to our modelling results. Our results for the MH agree relatively well with the more recent modelling work by Liu and Jiang (2016) who used the output of CMIP5-PMIP3 MH experiments to diagnose seasonal frost and permafrost extents, and active layer thicknesses in comparison to the PI. While all individ-

ual models investigated by Liu and Jiang (2016) show a relative reduction of permafrost areas for the MH (ranging between 1.8 % and 19.0 %) and a relative increase in seasonal frost areas, our simulations show a relative increase in permafrost area of 3.2 % and a relative increase in seasonal frost area by 3.4 %. Consistent with the model-ensemble mean by Liu and Jiang (2016), we simulated deeper active layers (relative increase by 1.9 %) for the MH compared to the PI. Besides slightly different ways of diagnosing the seasonal frost and permafrost compared to Liu and Jiang (2016), the main difference of increased MH permafrost extent in our simulations can be attributed to the colder MH climate relative to the PI simulated by AWI-ESM-2.5 (Table 1).

As for the MH, our simulations are in contrast to the much-reduced LIG permafrost extent in Eurasia suggested

by earlier modelling by Anisimov and Nelson (1996). As for the MH, the mean global surface warming of 2 °C for the LIG compared to the modern climate assumed by Anisimov and Nelson (1996) is exceeding more recent estimates of the LIG-PI global temperature anomalies (including +0.62 K (tropical sea surface temperature proxies; Bova et al. (2021)); +0.5 K (global sea surface temperature proxies; Hoffman et al. (2017)); −0.2 K (PMIP4-CMIP6 multimodel mean; Otto-Bliesner et al. (2021))). For comparison, the LIG-PI global temperature anomaly in our AWI-ESM-2.5 experiments amounts to −0.16 K which is again similar to the lower end of more recent estimates (Table 1). Despite the reduced permafrost extent (Fig. 4i) and increased thaw depths (Fig. 6i) across Eurasia simulated for the LIG, our results do not reproduce the magnitude of regional warming and permafrost thaw in Arctic Siberia reported by Schirrmeister et al. (2025). For North America during the LIG, Reyes et al. (2010) suggest widespread surficial permafrost thaw also within the current continuous and discontinuous permafrost regions, while deeper ice wedges were preserved and still persist until today. Similarly, Lauriol et al. (1997) suggested permafrost persistence in the northern Yukon during the Quaternary period. These findings align well with ours, that (i) permafrost as diagnosed via the temperature in 10 m depth persisted in northern North America during the LIG (Fig. 4i), while (ii) thaw depths were substantially deeper, potentially triggering surficial thaw as manifested in features such as thaw slumps or thaw lakes. However, the deep permafrost might also have persisted during a warm LIG climate due to ecosystem factors such as a protective vegetation (forest) cover, which is only indirectly represented via $n_t$-factors in our model.

The simulated MH and LIG permafrost probabilities are broadly consistent with speleothem-based permafrost proxies compiled from different sources (Kaushal et al., 2024; Biller-Celander et al., 2021; Vaks et al., 2013, 2020) (Fig. 3). Our simulations for the MH and LIG are consistent with the North American speleothem records discussed in Biller-Celander et al. (2021), but a more recent study by Batchelor et al. (2024) reports speleothem growth for a cave on the Nahanni plaetau in northwestern Canada during the LIG (Marine Isotope Stage (MIS) 5e). Due to the sparse spatial coverage, the speleothem records do not provide a tight spatial constraint, and an actual northward-shift of the permafrost zones during both the MH and LIG is well possible. Similarly, the persistence of permafrost in the Lenskaya Ledyanaya cave in Siberia since MIS-11 (Vaks et al., 2013) is consistent with our simulations, suggesting permafrost presence in that region during the current and last interglacial. Thus, or simulations of relatively stable permafrost presence in 10 m depth during the MH and LIG, broadly align with the interpretations of Biller-Celander et al. (2021) and Vaks et al. (2020) that circum-polar permafrost became increasingly persistent over the Pleistocene, while speleothem growth periods associated with deep permafrost thaw date

back to at least MIS-11 in Northern Yukon caves and Ledyana Lenskaya cave in central Siberia, and largely to MIS-9 and MIS-11 in caves on the Nahanni plateau northwestern Canada. These changes in permafrost persistence over the Pleistocene have been linked to increasing summer sea ice extents, hindering heat and moisture transport from the Arctic ocean towards the terrestrial Arctic (Lawrence et al., 2008; Vaks et al., 2020).

For the southern Tibetan plateau, our simulations suggested continuous permafrost during both MH and LIG, while the speleothems in the Tianmen cave are showing growth. This might be explained by the location of the cave in a valley surrounded by high mountain ranges. The extreme spatial variability of surface temperatures associated with the topography is not captured by the AWI-ESM-2.5/CryoGridLite setup. However, it might also be linked to transient climatic effects not captured by our equilibrium simulations, as suggested by Yan et al. (2025). Generally, various processes on glacial–interglacial time scales such as ecological and vegetation succession (Treat et al., 2019), carbon cycle responses (Lindgren et al., 2018), changing atmospheric or oceanic circulation patterns (Yan et al., 2025) and associated changes in precipitation and snow (Löfverström et al., 2014) are potentially affecting interglacial permafrost characteristics.

Overall, exceeding most previous estimates, our simulated interglacial continuous permafrost areas are probably slightly overestimated. At the same time, the transition from discontinuous to sporadic to isolated permafrost is relatively sharp and hence the non-continuous permafrost areas tend to be underestimated in our simulations. On the model-side, this and other deviations from observations and proxy records can be related to various factors including

i. surface temperatures biases in northern high latitude (in particular over land areas) simulated by AWI-ESM-2.5 (as documented for its predecessor AWI-ESM-1-1-LR (Brierley et al., 2020; Otto-Bliesner et al., 2021)),

ii. missing or overly simplified process representations in CryoGridLite (e.g., no soil-freezing characteristic, no dynamic soil hydrology),

iii. the parameter-ensemble not representing the actual variability of surface temperatures and environmental conditions within a grid cell (for example in mountainous terrain),

iv. equilibrium climate simulations not capturing transient climate effects such as ecosystem-protected permafrost occurrence at the southern limits of the northern permafrost region (e.g. central Quebec), and

v. inaccuracies related to the way permafrost is diagnosed from the model output (Steinert et al., 2023).

Despite these limitations and uncertainties, our approach allows to draw conclusions about the general influences of the

mean temperature versus the seasonal temperature amplitude on the ground thermal dynamics and associated processes.

## 4.2 How temperature seasonality drives interglacial permafrost dynamics

### 4.2.1 Implications for reconstructions of paleo-climates and -environments

The mean surface temperature turned out to exert the dominant control on the presence of permafrost. This finding is consistent with the approaches of Gruber (2012) and Chadburn et al. (2017) who derived robust, observation-based relations between the local mean annual air temperature and the probability of equilibrium permafrost occurrence. These works and our findings suggest a robust coupling between mean ground temperatures and the near-surface air temperatures under equilibrium conditions. However, these works have in common, that they cannot diagnose transient effects such as disequilibrium or relict permafrost (Opel et al., 2024) which can be present in great depths or locations with highly-insulating surface covers (ecosystem-protected permafrost) such as in larch taiga, where also long-term vegetation–fire–permafrost–climate feedbacks play a role (Dietze et al., 2020; Stuenzi et al., 2022). With respect to reconstructions of past interglacial climates and paleo environments, our results suggest a close link between the mean surface temperatures and the presence or absence of permafrost, which would generally allow to derive information about permafrost presence from annual temperature proxies. However, our findings also underline the importance that proxies must be reflective of annual mean temperature conditions and not biased towards seasons in order to establish reliable links. Proxies that are biased towards either summer or winter season might actually reflect differences in temperature seasonality instead of different means (Kwiecien et al., 2022). For example, reconstructions of permafrost extent based on plant macrofossils or pollen, could be biased towards the growing season (Bova et al., 2021), and therefore suggest the absence of permafrost during past interglacials, even though colder winters could still compensate and allow for permafrost presence. This seasonal bias problem can partly explain the differences between earlier proxy-based reconstructions suggesting marked interglacial permafrost retreat (Zoltai, 1995), and more recent works including ours suggesting interglacial permafrost persistence at depth (Reyes et al., 2010; Biller-Celander et al., 2021).

According to our simulations, maximum annual thaw depths are positively correlated to both, the mean and the seasonality of surface temperatures. This finding is consistent with theoretical considerations and simple models like the Stefan model for which thaw depths increase with the number of thawing degrees days which in turn increase with both higher mean temperatures and larger seasonal amplitudes (Riseborough et al., 2008). Therefore, substantially higher thaw depths compared to PI conditions can be expected under the higher seasonal amplitudes of the MH and LIG climates, even if the mean temperatures would be similar to PI levels (Fig. 6a, d, g). As warmer summers and higher thaw depths can initiate thermokarst (e.g. thaw lake formation) and thermo-erosion (e.g. retrogressive thaw slumps) even in cold permafrost (Farquharson et al., 2019; Jones et al., 2019), a high abundance of these features, for example during the early and the mid Holocene (Brosius et al., 2021), does not necessarily require higher mean annual temperatures, but can also be caused by warm summers associated with marked seasonal temperature amplitudes. In our AWI-ESM simulations, the MH and LIG climates are even colder than the PI in northern North America and on the Tibetan plateau (Fig. 1), which seemingly contradicts reconstructions of substantial near-surface thaw compared to today during these interglacial climates (Reyes et al., 2010). However, in the simulations, the effect of higher seasonal temperature amplitudes on thaw depths compensates for the colder mean temperatures during the MH, and exceeds it during the LIG, resolving the seeming contradiction. Thus, past periods of enhanced surficial permafrost thaw during interglacials evident from the occurrence of thermokarst and thermo-erosion features could at least partly be attributed to the larger seasonal temperature amplitude during those times, and do not necessarily require substantially higher mean temperatures. Similarly, equilibrium permafrost extent might not have been substantially reduced compared to present conditions, since deep permafrost might have been resilient to surficial thaw, consistent with findings of increasing permafrost persistence through the late Pleistocene (Reyes et al., 2010; Biller-Celander et al., 2021). Nevertheless, multi-proxy climate reconstructions for the LIG in northeastern Siberia suggest a markedly warmer average climate than our simulations which cannot be ascribed to the effects of enhanced seasonality or saonsal biases in the proxies alone (Schirrmeister et al., 2025).

Besides its positive correlation with seasonal thaw depths, we found the temperature seasonality to almost exclusively determine the abundance of thermal contraction cracking during the MH and LIG, with higher seasonal amplitudes implying more frequent cracking. As thermal contraction cracking activity drives the formation and growth of ice wedges, it is also a first-order indicator of excess ice accumulation (Bockheim and Hinkel, 2012), which can be considered as a stabilizing process for permafrost, at least on decadal time scales (Jorgenson et al., 2015; Kanevskiy et al., 2017). On centennial to millennial time scales, high excess ice contents do, however, increase the vulnerability of the landscape to the occurrence of rapid thaw processes like thermokarst (Kokelj and Jorgenson, 2013). Therefore, the occurrence of thermokarst during past interglacials could at least partly be associated with a generally more active "ground ice cycling" compared to recent condition, especially in continental regions with a higher seasonal temperature amplitude. With

respect to past climate and environment reconstructions, our diagnostic for thermal contraction cracking (Figs. 7 and A3) based on the comprehensive observations and synthesis by Matsuoka et al. (2018) can be directly linked to the occurrence of ice-wedges, ice-wedge casts, and potentially sand wedges (Black, 1976; Wolfe et al., 2018). Below the mean annual temperatures required for permafrost occurrence, our results indicate an absence of a strong control of the mean annual temperature on deep thermal contraction cracking activity, suggesting that observations of ice-wedge casts or sand wedges should not be used to reconstruct mean air temperatures which is in line with earlier findings (Murton and Kolstrup, 2003; Christiansen et al., 2016). The occurrence of deep thermal contraction cracking was well aligned with the simulated permafrost domain (Fig. 7), confirming that past permafrost limits and periglacial conditions can be reconstructed based on the occurrence of deep ice-wedge casts (Stadelmaier et al., 2021). However, conditions favourable for shallow thermal-contraction cracking are also found outside the permafrost domain yet within the seasonal frost domain (Fig. A3), which has to be kept in mind when interpreting ice-wedge or sand-wedge casts.

Overall, our results suggest more active excess ground ice dynamics during the MH and LIG compared to recent conditions, and potentially also during further past interglacials. This can be attributed to increased seasonal temperature amplitudes which on the one hand lead to more abundant thermal contraction cracking and thus enhanced ground-ice accumulation in form of ice wedges during winter, and on the other hand cause deeper thaw during summer, making the initiation of rapid thaw processes like thermokarst and thermoerosion more likely. These effects should be considered in proxy-based reconstructions of paleo climate and environments based on ground-ice related proxies.

### 4.2.2 Implications for the permafrost response to ongoing and future climate change

Beyond the implications for reconstructions of past climates, it is instructive to contextualize our findings with respect to projections of future climate change. While the differences between the past interglacial climates of the MH and LIG compared to the PI are primarily driven by different orbital configurations (Table 1), the currently ongoing and near-future climate change is happening on decadal to centennial time scales and thus solely driven by a rapidly changing greenhouse gas forcing. Accordingly, the MH and LIG climates in the AWI-ESM and other ESMs (Brierley et al., 2020; Otto-Bliesner et al., 2021) are characterized by a substantially higher temperature seasonality, but relatively modest patterns of regional cooling and warming (Fig. 1). Conversely, the near-future climates are characterized by marked temperature increases, in particular in the high latitudes (Rantanen et al., 2022). At the same time, asymmetric seasonal warming trends due to more rapid winter warming
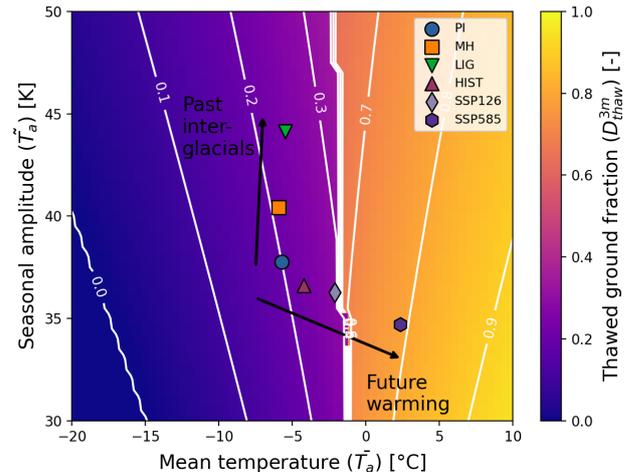


**Figure 8.** Scatter plot of the mean annual temperature ($\overline{T}_a$) and temperature seasonality ($\tilde{T}_a$) averaged over the joint permafrost domain for different climate states simulated with AWI-ESM-2 (PI: pre-industrial; MH: mid Holocene; LIG: last interglacial; HIST: historical (1990–2014); SSP126: Shared socio-economic pathway scenario 1–2.6 (2075–2099); SSP126: Shared socio-economic pathway scenario 5–8.5 (2075–2099)). The background shows the annual thawed ground fraction within the upper 3 m of the subsurface ($D_{thaw}^{3m}$) according to the Stefan model (see Appendix B for details).

(Bintanja and van der Linden, 2013) are likely to lead to a decrease in temperature seasonality under both the SSP1-2.6 and SSP5-8.5 scenarios, overall setting the future climate on a trajectory much different from the states experiences during past interglacials (Fig. 8).

To highlight implications of these contrasting climate trajectories, we derived an analytical estimate of the annual thawed ground fraction ($D_{thaw}^{3m}$) based on the Stefan model (see Appendix B; Fig. 8). Relative to the PI state, both an increase in seasonality as well as an increase in mean temperatures would lead to an increase in thawed ground fraction on average. However, while the increase is relatively small for the past interglacials, the current and near-future climate trajectory (from PI over HIST to the SSPs) corresponds to the most rapid increase, as it is oriented perpendicular to the isolines of $D_{thaw}^{3m}$. Our results further indicate that with decreasing seasonality of the projected near-future climate trajectory, the thermal contraction cracking activity is going to decrease, while it was higher during the MH and LIG interglacials. Thus, excess ice accumulation and the associated short-term stabilization of permafrost is becoming less likely in the near future.

Overall, our findings suggest that with respect to permafrost dynamics, the most recent interglacial climates of the MH and LIG can, if at all, only partly serve as analogues for the changes to be expected under the current and near-future climate trajectory. While the abundance of surficial permafrost thaw in those past periods can partly be attributed to the effects of a higher temperature seasonal-

ity and thus warmer summers and deeper seasonal thaw, the current and future thaw is driven by year-round warming, which is particularly pronounced in winter (Rantanen et al., 2022). This will eventually result in permafrost thaw at depth and a marked decline in the overall permafrost extent, likely exceeding thaw magnitudes in previous interglacials where deep permafrost was resilient to thaw (Biller-Celander et al., 2021). The already observed circum-Arctic intensification of fire regimes could further contribute to active-layer thickening and permafrost thaw during summers in the near future (Li et al., 2022; Jiang et al., 2023; Diaz et al., 2024), but also permafrost thaw could feed back to further intensify fires via more rapid soil drying (Kim et al., 2024). In addition, sea-ice decline on a trajectory to an ice-free Arctic during summer (Guarino et al., 2020; Vermassen et al., 2023; Jahn et al., 2024) could drive further permafrost thaw through increased ocean-to-land heat and moisture transport (Lawrence et al., 2008; Vaks et al., 2020; Nitzbon et al., 2024). Consequently, we anticipate the northern permafrost region to experience climatic conditions in the future, which are likely associated with a decline in permafrost extent, deeper seasonal thaw and thus higher likelihood of abrupt thaw initiation, less potential for landscape stabilization through excess ice accumulation, and longer exposures of soil carbon to thawed conditions. Such climatic conditions are unprecedented since at least MIS-11 (about 400 ka BP), and more suitable analogues for future permafrost dynamics, in particular under high-emission scenarios, might even date back to the mid-Pliocene warm period (about 3 Ma BP) (Guo et al., 2023), in line with Burke et al. (2018). Recent evidence from speleothems in the Lena River delta (dated to about 8.7 Ma BP) has also suggested that the Tortonian stage of the Late Miocene could be a more suitable analog for near-future climate warming under high-emission scenarios (Umbo et al., 2025).

The current climate trajectory will induce permafrost loss and irreversible landscape changes in northern high-latitude land areas. Despite the anticipated gradual response of permafrost to climate warming on the global scale (Nitzbon et al., 2024), these changes can amplify permafrost–climate feedbacks, and might lead to the crossing of Arctic climate thresholds (Brovkin et al., 2025) which is a key subject of ongoing modelling efforts (Cui et al., 2025; Winkelmann et al., 2025).

## 5 Conclusions

We have conducted parameter-ensemble simulations of ground thermal characteristics using the CryoGridLite permafrost model, driven by pre-industrial (PI), mid-Holocene (MH), and last interglacial (LIG) climate forcing time series from the AWI-ESM-2.5 coupled climate model, based on PMIP4 boundary conditions. From the presented results, we draw the following conclusions:

1. The simulated permafrost extent using AWI-ESM-2.5/CryoGridLite is in good agreement with speleothem- and pollen-based reconstructions for the MH and LIG. However, there is a consistent tendency to overestimate permafrost extent, likely due to a cold bias in northern high-latitude surface temperatures in the AWI-ESM-2.5 simulations.

2. Compared to the PI, permafrost extent increased slightly during the MH ($+3\%$) and decreased during the LIG ($-5\%$). Maximum thaw depth increased during both the MH ($+2\%$) and LIG ($+12\%$). Thermal contraction cracking activity showed substantial increases during the MH ($+32\%$) and LIG ($+79\%$), with strong regional signals in northern and southern Siberia.

3. Regional responses to interglacial climate forcing differ significantly. In northern Eurasia, increased mean temperatures and higher seasonal amplitudes lead to greater thaw depths, while in North America and southern Eurasia, opposing effects of these variables tend to offset each other.

4. Mean annual temperature and seasonal temperature amplitude influence different aspects of permafrost and seasonally frozen ground. Permafrost probability is primarily governed by annual mean temperatures, whereas thermal contraction cracking activity is almost exclusively controlled by seasonal temperature amplitude.

5. Reconstructions of near-surface permafrost thaw during past interglacials can largely be explained by increased thaw depths driven by elevated seasonal temperature amplitudes, without necessarily requiring higher mean annual temperatures or extensive deep permafrost loss.

Given that the Arctic's projected climate trajectory involves rising mean temperatures alongside decreasing seasonal temperature amplitude (Fig. 8), past interglacials offer only limited analogues for future permafrost dynamics and associated feedbacks. Instead, we may expect permafrost thaw trajectories during the 21st century that are unprecedented since at least Marine Isotope Stage 11 (approximately 400 000 years ago).

## Appendix A: Additional diagnostics

In addition to the diagnostics described in Sect. 2.2.3, we complemented our analysis by the following quantities.

– We diagnosed the *seasonal frost probability* ($p_{SF}$) as the fraction of ensemble members for which the minimum annual temperature in 1 m depths is below $0\,°C$, i.e. frost regularly penetrates down to a depth of 1 m. The overall seasonal frost area (including the permafrost area) was obtained as $\Omega_{SF} = \sum_{x,y} p_{SF}\omega(x,y)$.

Based on the simulated seasonal frost probabilities, we defined the joint seasonal frost domain as all grid cells for which $p_{SF} > 0$ or $p_{PF} > 0$ in any of the nine simulations. For the joint seasonal frost domain, we further diagnosed the following quantities, providing further insights into the ground thermal regime beyond the permafrost domain:

- Following Harp et al. (2016), we additionally diagnosed the annual thawed ground fraction ($D_{thaw}^{3\,m}$) as the depth- and time-integrated fraction of thawed ground within the upper 3 m of the subsurface over the period of one year. While the thawed ground fraction $D_{thaw}^{3\,m} \in [0, 1]$ is harder to retrieve from field observations than thaw depths, it is more informative as a first-order approximation of conditions favourable for microbial decomposition of organic matter. For Fig. 8, we derived a simple approximation of this quantity, based on the Stefan equation (see Appendix B).

- Similar to the deep thermal contraction cracking, we diagnosed the *shallow thermal contraction cracking activity* ($a_{FC}^{shallow}$ (d yr$^{-1}$)), but used different thresholds of $T_{1\,m} < -5\,°C$ and $\nabla T_{1\,m} > 7\,°C\,m^{-1}$ (i.e., $T_{0\,m} < T_{1\,m} - 7\,°C$). Shallow thermal contraction cracking can also occur outside permafrost-affected areas.

The corresponding results for these diagnostics are provided in Figs. A1, A2, and A3 below.
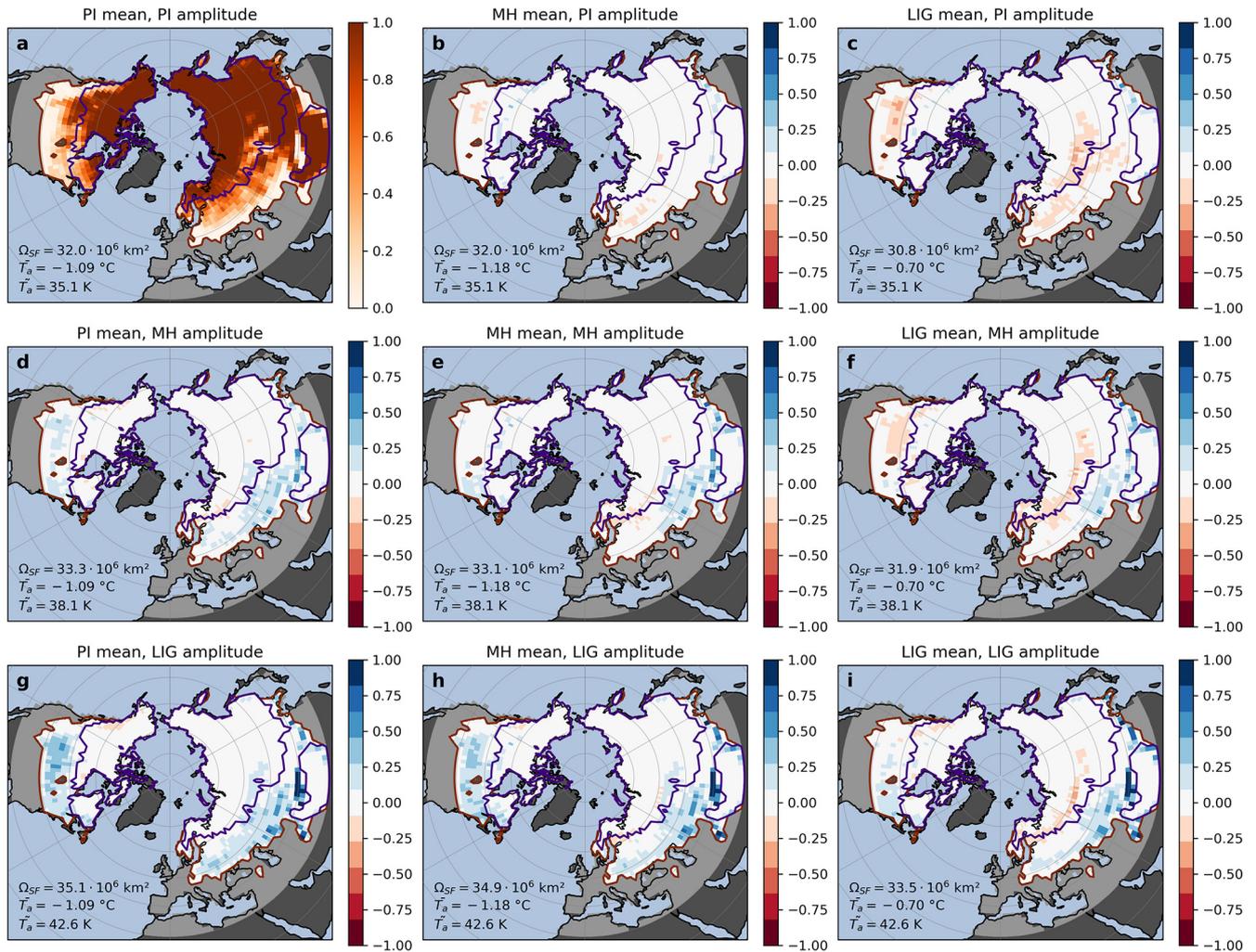
**Figure A1.** Simulated seasonal frost probabilities ($p_{SF}$) for all climate forcings, shown as absolute values for the PI experiment in panel **(a)**, and as anomalies for all other experiments. The results for the original climate forcings are shown on the diagonal (PI: **(a)**; MH: **(e)**; LIG: **(i)**), and the off-diagonal panels show results for the alternative climate forcings, with each column having the same mean temperature (PI: **(a)**, **(d)**, **(g)**; MH: **(b)**, **(e)**, **(h)**; LIG: **(c)**, **(f)**, **(i)**) and each row having the same temperature amplitudes (PI: **(a)**, **(b)**, **(c)**; MH: **(d)**, **(e)**, **(f)**; LIG: **(g)**, **(h)**, **(i)**). The purple (orange) line marks the limits of the joint permafrost (seasonal frost) domain of all simulations. The seasonal frost extent ($\Omega_{SF}$), the mean annual temperature ($\overline{T_a}$), and the mean temperature amplitude ($\tilde{T}_a$) for the joint seasonal frost domain are given in the lower left corner of each panel.
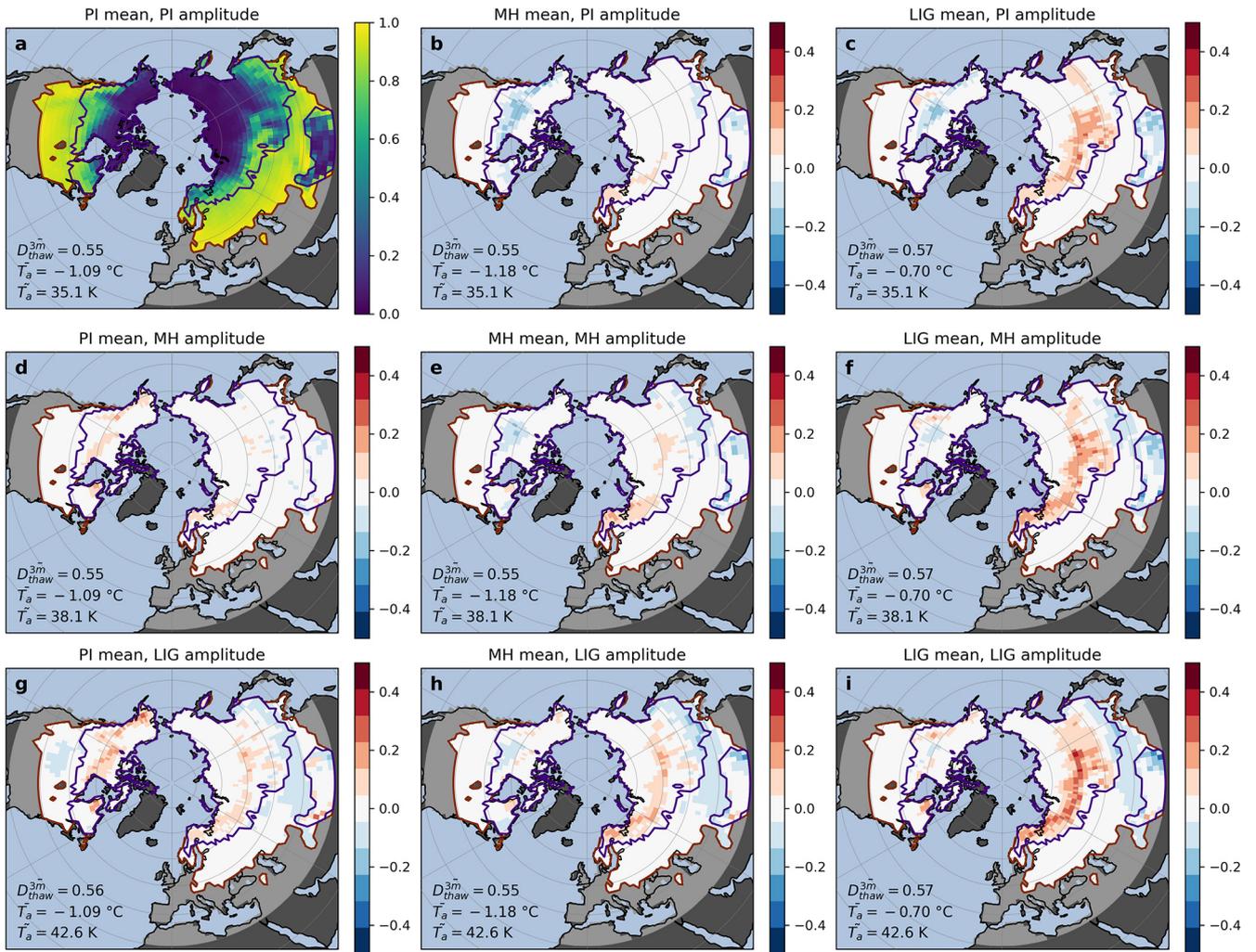
**Figure A2.** Same as Fig. A1, but for the annual thawed ground fraction ($D_{thaw}^{3\,m}$). The mean annual thawed ground fraction ($\overline{D_{thaw}^{3\,m}}$), the mean annual temperature ($\overline{T_a}$), and the mean temperature amplitude ($\tilde{T}_a$) for the joint seasonal frost domain are given in the lower left corner of each panel.
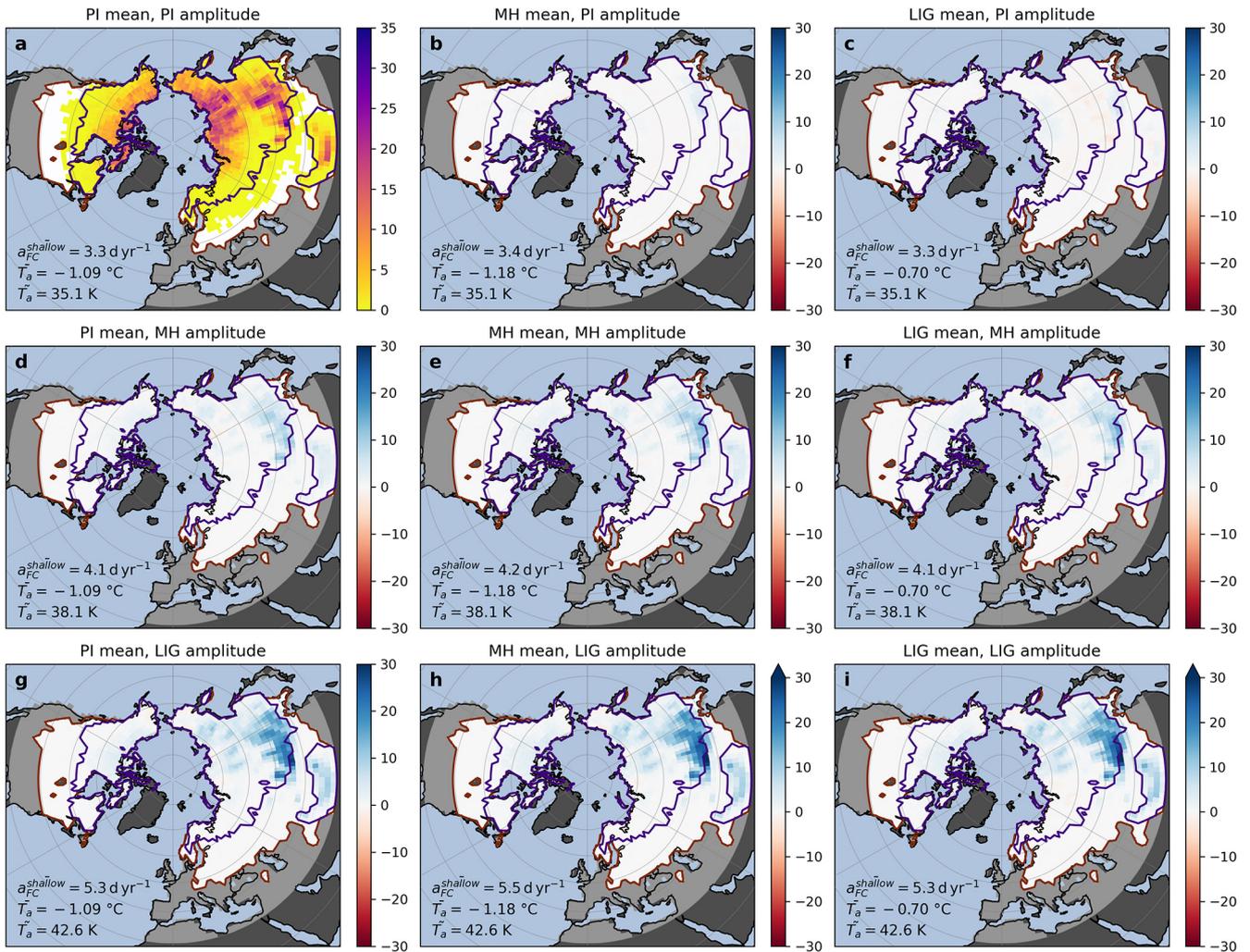
**Figure A3.** Same as Fig. A1, but for the shallow thermal contraction cracking activity ($a_{\mathrm{FC}}^{\mathrm{shallow}}$). The mean shallow thermal contraction cracking activity ($\overline{a_{\mathrm{FC}}^{\mathrm{shallow}}}$), the mean annual temperature ($\overline{T_a}$), and the mean temperature amplitude ($\tilde{T}_a$) for the joint seasonal frost domain are given in the lower left corner of each panel.

## Appendix B: Calculation of annual thawed ground fraction using the Stefan model

For Fig. 8 we calculated the annual thawed ground fraction ($D_{\text{thaw}}^d$) within the upper $d = 3$ m of the subsurface in dependence of the mean ($\overline{T_a}$) and the seasonal amplitude ($\tilde{T}_a$) of the surface temperature using the Stefan model (Riseborough et al., 2008). For this, we assumed the annual temperature evolution to have a sinusoidal shape:

$$T_a(t) = \overline{T_a} + \frac{\tilde{T}_a}{2} \cdot \sin\left(2\pi \frac{t}{P}\right) \tag{B1}$$

where $t$ is the time and $P = 365$ d is the period length (Fig. B1a).

The thawing (freezing) index $I_{\text{t}|\text{f}}(t)$ was determined as the integral over the positive (negative) surface temperature, scaled using a thawing (freezing)-season $n$-factor ($n_{\text{t}|\text{f}}$). The integration limits were set to start at the first root of the temperature curve at $t_0 = -\frac{2\pi}{P} \arcsin\left(\frac{2\overline{T_a}}{\tilde{T}_a}\right)$ (Fig. B1a, b):

$$I_t(t) = n_t \int_{t_0}^{t} T_a(t')\big|_{T_a>0} \, dt' \tag{B2}$$

$$I_f(t) = -n_f \int_{t_0}^{t} T_a(t')\big|_{T_a<0} \, dt' \tag{B3}$$

With these, the progression of the thaw (freeze) front $X_{\text{t}|\text{f}}(t)$ was determined using the Stefan equation (Fig. B1c):

$$X_{\text{t}|\text{f}}(t) = \sqrt{\frac{2\,k_{\text{t}|\text{f}}\,I_{\text{t}|\text{f}}(t)}{\theta\,\phi\,L_{\text{sl}}}} \tag{B4}$$

where $L_{\text{sl}} = 334 \times 10^6$ J m$^{-3}$ is the volumetric latent heat of fusion of water, $\theta$ the water/ice saturation of the sediment's pore space, $\phi$ the sediment's porosity. $k_{\text{t}|\text{f}}$ refers to the thawed/frozen ground thermal conductivity parameterized as follows:

$$k_{\text{t}|\text{f}} = \left(\theta\phi\sqrt{k_{\text{w}|\text{i}}} + (1 - \phi)\sqrt{k_s}\right)^2 \tag{B5}$$

with the constituents' thermal conductivities set to $k_s = 3.0$ W K$^{-1}$ m$^{-1}$ for the sediment, $k_i = 2.2$ W K$^{-1}$ m$^{-1}$ for ice, and $k_w = 0.57$ W K$^{-1}$ m$^{-1}$ for water.

The Stefan model indicates thermally stable permafrost, if the maximum freeze depth exceeds the maximum thaw depth over the course of one year ($X_f(t_0 + P) > X_t(t_0 + P)$); otherwise there is no permafrost. For the permafrost case, the annual thawed ground fraction $D_{\text{thaw}}^d$ was obtained by integrating the difference between the thaw and freeze fronts between $t = t_0$ and the point $t = t_1$ where the freeze front reaches the thaw front, and normalizing by the maximum depth $d$ and temporal period $P$ (Fig. B1c):

$$D_{\text{thaw}}^d = \frac{\int_{t_0}^{t_1} \min\left[d, X_t(t') - X_f(t')\right] \, dt'}{d\,P}$$
$$\text{if} \quad X_f(t_0 + P) > X_t(t_0 + P) \quad \text{(permafrost)} \tag{B6}$$

For the case of no permafrost, the freeze and thaw fronts were shifted such that the freezing starts at $t = t_0$. Then, $D_{\text{thaw}}^d$ was obtained by first determining the annual frozen ground fraction through a similar integration as above, and then subtracting it from 1:

$$D_{\text{thaw}}^d = 1 - \frac{\int_{t_0}^{t_1} \min\left[d, X_f(t') - X_t(t')\right] \, dt'}{d\,P}$$
$$\text{if} \quad X_f(t_0 + P) \leq X_t(t_0 + P) \quad \text{(no permafrost)} \tag{B7}$$

Note that $D_{\text{thaw}}^d = 0$ if $\overline{T_a} + \frac{\tilde{T}_a}{2} < 0$, and $D_{\text{thaw}}^d = 1$ if $\overline{T_a} - \frac{\tilde{T}_a}{2} > 0$. For Fig. 8 we set $n_t = 1.0$, $n_f = 0.5$, $\phi = 0.5$, and $\theta = 0.75$, such that $k_t \approx 1.32$ W K$^{-1}$ m$^{-1}$ and $k_f \approx 2.02$ W K$^{-1}$ m$^{-1}$.
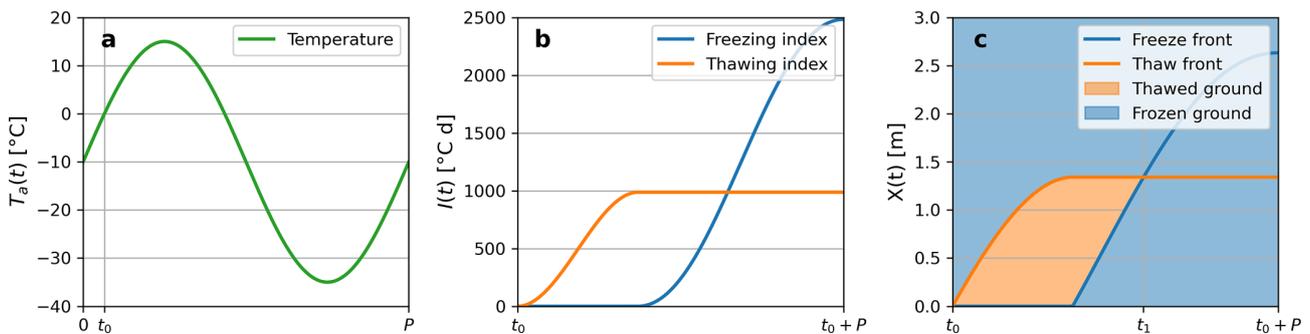


**Figure B1.** Illustration of how the thawed ground fraction ($D_{\text{thaw}}^d$ was obtained using the Stefan model. **(a)** We assumed a sinusoidal temperature curve $T_a(t)$ of mean $\overline{T_a}$ and amplitude $\tilde{T}_a$. **(b)** Thawing (freezing) indices ($I_{\text{t}|\text{f}}(t)$ were obtained by integrating the positive (negative) temperatures and scaling them using $n$-factors. **(c)** The thawed ground fraction was obtained by integrating the difference between the thaw and freeze fronts ($X_{\text{t}|\text{f}}$), and normalizing it by the depth $d$ and period of one year ($P$).

# References

Anisimov, O. A. and Nelson, F. E.: Permafrost distribution in the Northern Hemisphere under scenarios of climatic change, Global and Planetary Change, 14, 59–72, https://doi.org/10.1016/0921-8181(96)00002-1, 1996.

Batchelor, C. J., Orland, I. J., Marcott, S. A., Slaughter, R., Edwards, R. L., Zhang, P., Li, X., and Cheng, H.: Distinct Permafrost Conditions Across the Last Two Glacial Periods in Midlatitude North America, Geophys. Res. Lett., 46, 13318–13326, https://doi.org/10.1029/2019GL083951, 2019.

Batchelor, C. J., McGee, D., Shakun, J. D., Woodhead, J., Jost, A. B., Arnold, S., Horne, G., Kinsley, C. W., and Freudenburg-Puricelli, M.: Insights Into Changing Interglacial Conditions in Subarctic Canada From MIS 11 Through MIS 5e From Seasonally Resolved Speleothem Records, Geophys. Res. Lett., 51, e2024GL108459, https://doi.org/10.1029/2024GL108459, 2024.

Biller-Celander, N., Shakun, J. D., McGee, D., Wong, C. I., Reyes, A. V., Hardt, B., Tal, I., Ford, D. C., and Lauriol, B.: Increasing Pleistocene permafrost persistence and carbon cycle conundrums inferred from Canadian speleothems, Science Advances, 7, eabe5799, https://doi.org/10.1126/sciadv.abe5799, 2021.

Bintanja, R. and van der Linden, E. C.: The changing seasonal climate in the Arctic, Scientific Reports, 3, 1556, https://doi.org/10.1038/srep01556, 2013.

Black, R. F.: Periglacial features indicative of permafrost: Ice and soil wedges, Quaternary Research, 6, 3–26, https://doi.org/10.1016/0033-5894(76)90037-5, 1976.

Bockheim, J. G. and Hinkel, K. M.: Accumulation of Excess Ground Ice in an Age Sequence of Drained Thermokarst Lake Basins, Arctic Alaska, Permafrost and Periglacial Processes, 23, 231–236, https://doi.org/10.1002/ppp.1745, 2012.

Bova, S., Rosenthal, Y., Liu, Z., Godad, S. P., and Yan, M.: Seasonal origin of the thermal maxima at the Holocene and the last interglacial, Nature, 589, 548–553, https://doi.org/10.1038/s41586-020-03155-x, 2021.

Brierley, C. M., Zhao, A., Harrison, S. P., Braconnot, P., Williams, C. J. R., Thornalley, D. J. R., Shi, X., Peterschmitt, J.-Y., Ohgaito, R., Kaufman, D. S., Kageyama, M., Hargreaves, J. C., Erb, M. P., Emile-Geay, J., D'Agostino, R., Chandan, D., Carré, M., Bartlein, P. J., Zheng, W., Zhang, Z., Zhang, Q., Yang, H., Volodin, E. M., Tomas, R. A., Routson, C., Peltier, W. R., Otto-Bliesner, B., Morozova, P. A., McKay, N. P., Lohmann, G., Legrande, A. N., Guo, C., Cao, J., Brady, E., Annan, J. D., and Abe-Ouchi, A.: Large-scale features and evaluation of the PMIP4-CMIP6 *midHolocene* simulations, Clim. Past, 16, 1847–1872, https://doi.org/10.5194/cp-16-1847-2020, 2020.

Brosius, L. S., Anthony, K. M. W., Treat, C. C., Lenz, J., Jones, M. C., Bret-Harte, M. S., and Grosse, G.: Spatiotemporal patterns of northern lake formation since the Last Glacial Maximum, Quaternary Science Reviews, 253, 106773, https://doi.org/10.1016/j.quascirev.2020.106773, 2021.

Brovkin, V., Bartsch, A., Hugelius, G., Calamita, E., Lever, J. J., Goo, E., Kim, H., Stacke, T., and de Vrese, P.: Permafrost and Freshwater Systems in the Arctic as Tipping Elements of the Climate System, Surveys in Geophysics, https://doi.org/10.1007/s10712-025-09885-9, 2025.

Burke, K. D., Williams, J. W., Chandler, M. A., Haywood, A. M., Lunt, D. J., and Otto-Bliesner, B. L.: Pliocene and

Eocene provide best analogs for near-future climates, Proceedings of the National Academy of Sciences, 115, 13288–13293, https://doi.org/10.1073/pnas.1809600115, 2018.

Cai, Y., Cheng, H., An, Z., Edwards, R. L., Wang, X., Tan, L., and Wang, J.: Large variations of oxygen isotopes in precipitation over south-central Tibet during Marine Isotope Stage 5, Geology, 38, 243–246, https://doi.org/10.1130/G30306.1, 2010.

Cai, Y., Zhang, H., Cheng, H., An, Z., Lawrence Edwards, R., Wang, X., Tan, L., Liang, F., Wang, J., and Kelly, M.: The Holocene Indian monsoon variability over the southern Tibetan Plateau and its teleconnections, Earth and Planetary Science Letters, 335-336, 135–144, https://doi.org/10.1016/j.epsl.2012.04.035, 2012.

Chadburn, S. E., Burke, E. J., Cox, P. M., Friedlingstein, P., Hugelius, G., and Westermann, S.: An observation-based constraint on permafrost loss as a function of global warming, Nature Climate Change, 7, 340–344, https://doi.org/10.1038/nclimate3262, 2017.

Christiansen, H. H., Matsuoka, N., and Watanabe, T.: Progress in Understanding the Dynamics, Internal Structure and Palaeoenvironmental Potential of Ice Wedges and Sand Wedges, Permafrost and Periglacial Processes, 27, 365–376, https://doi.org/10.1002/ppp.1920, 2016.

Crichton, K. A., Bouttes, N., Roche, D. M., Chappellaz, J., and Krinner, G.: Permafrost carbon as a missing link to explain CO2 changes during the last deglaciation, Nature Geoscience, 9, 683–686, https://doi.org/10.1038/ngeo2793, 2016.

Cui, M., Ji, D., and Chen, Y.: Permafrost response and feedback under temperature stabilization and overshoot scenarios with different global warming levels, Earth Syst. Dynam., 16, 1809–1831, https://doi.org/10.5194/esd-16-1809-2025, 2025.

Denniston, R. F. and Luetscher, M.: Speleothems as high-resolution paleoflood archives, Quaternary Science Reviews, 170, 1–13, https://doi.org/10.1016/j.quascirev.2017.05.006, 2017.

Diaz, L. R., Delcourt, C. J. F., Langer, M., Loranty, M. M., Rogers, B. M., Scholten, R. C., Shestakova, T. A., Talucci, A. C., Vonk, J. E., Wangchuk, S., and Veraverbeke, S.: Environmental drivers and remote sensing proxies of post-fire thaw depth in eastern Siberian larch forests, Earth Syst. Dynam., 15, 1459–1482, https://doi.org/10.5194/esd-15-1459-2024, 2024.

Dietze, E., Mangelsdorf, K., Andreev, A., Karger, C., Schreuder, L. T., Hopmans, E. C., Rach, O., Sachse, D., Wennrich, V., and Herzschuh, U.: Relationships between low-temperature fires, climate and vegetation during three late glacials and interglacials of the last 430 kyr in northeastern Siberia reconstructed from monosaccharide anhydrides in Lake El'gygytgyn sediments, Clim. Past, 16, 799–818, https://doi.org/10.5194/cp-16-799-2020, 2020.

Dublyansky, Y., Moseley, G. E., Lyakhnitsky, Y., Cheng, H., Edwards, L. R., Scholz, D., Koltai, G., and Spötl, C.: Late Palaeolithic cave art and permafrost in the Southern Ural, Scientific Reports, 8, 12080, https://doi.org/10.1038/s41598-018-30049-w, 2018.

Erb, M. P., McKay, N. P., Steiger, N., Dee, S., Hancock, C., Ivanovic, R. F., Gregoire, L. J., and Valdes, P.: Reconstructing Holocene temperatures in time and space using paleoclimate data assimilation, Clim. Past, 18, 2599–2629, https://doi.org/10.5194/cp-18-2599-2022, 2022.

FAO and ITPS: Global Soil Organic Carbon Map (GSOCmap), technical Report, FAO, Rome, ISBN 978-92-5-130439-6, 2018.

Farquharson, L. M., Romanovsky, V. E., Cable, W. L., Walker, D. A., Kokelj, S. V., and Nicolsky, D.: Climate Change Drives Widespread and Rapid Thermokarst Development in Very Cold Permafrost in the Canadian High Arctic, Geophys. Res. Lett., 46, 6681–6689, https://doi.org/10.1029/2019GL082187, 2019.

Geyh, M. A. and Heine, K.: Several distinct wet periods since 420 ka in the Namib Desert inferred from U-series dates of speleothems, Quaternary Research, 81, 381–391, https://doi.org/10.1016/j.yqres.2013.10.020, 2014.

González-Lemos, S., Müller, W., Pisonero, J., Cheng, H., Edwards, R. L., and Stoll, H. M.: Holocene flood frequency reconstruction from speleothems in northern Spain, Quaternary Science Reviews, 127, 129–140, https://doi.org/10.1016/j.quascirev.2015.06.002, 2015.

Groenke, B., Langer, M., Nitzbon, J., Westermann, S., Gallego, G., and Boike, J.: Investigating the thermal state of permafrost with Bayesian inverse modeling of heat transfer, The Cryosphere, 17, 3505–3533, https://doi.org/10.5194/tc-17-3505-2023, 2023.

Groenke, B., Langer, M., Miesner, F., Westermann, S., Gallego, G., and Boike, J.: Robust Reconstruction of Historical Climate Change From Permafrost Boreholes, Journal of Geophysical Research: Earth Surface, 129, e2024JF007734, https://doi.org/10.1029/2024JF007734, 2024.

Gruber, S.: Derivation and analysis of a high-resolution estimate of global permafrost zonation, The Cryosphere, 6, 221–233, https://doi.org/10.5194/tc-6-221-2012, 2012.

Guarino, M.-V., Sime, L. C., Schröeder, D., Malmierca-Vallet, I., Rosenblum, E., Ringer, M., Ridley, J., Feltham, D., Bitz, C., Steig, E. J., Wolff, E., Stroeve, J., and Sellar, A.: Sea-ice-free Arctic during the Last Interglacial supports fast future loss, Nature Climate Change, 10, 928–932, https://doi.org/10.1038/s41558-020-0865-2, 2020.

Guo, D., Wang, H., Romanovsky, V. E., Haywood, A. M., Pepin, N., Salzmann, U., Sun, J., Yan, Q., Zhang, Z., Li, X., Otto-Bliesner, B. L., Feng, R., Lohmann, G., Stepanek, C., Abe-Ouchi, A., Chan, W.-L., Peltier, W. R., Chandan, D., von der Heydt, A. S., Contoux, C., Chandler, M. A., Tan, N., Zhang, Q., Hunter, S. J., and Kamae, Y.: Highly restricted near-surface permafrost extent during the mid-Pliocene warm period, Proceedings of the National Academy of Sciences, 120, e2301954120, https://doi.org/10.1073/pnas.2301954120, 2023.

Harp, D. R., Atchley, A. L., Painter, S. L., Coon, E. T., Wilson, C. J., Romanovsky, V. E., and Rowland, J. C.: Effect of soil property uncertainties on permafrost thaw projections: a calibration-constrained analysis, The Cryosphere, 10, 341–358, https://doi.org/10.5194/tc-10-341-2016, 2016.

Herzschuh, U., Böhmer, T., Chevalier, M., Hébert, R., Dallmeyer, A., Li, C., Cao, X., Peyron, O., Nazarova, L., Novenko, E. Y., Park, J., Rudaya, N. A., Schlütz, F., Shumilovskikh, L. S., Tarasov, P. E., Wang, Y., Wen, R., Xu, Q., and Zheng, Z.: Regional pollen-based Holocene temperature and precipitation patterns depart from the Northern Hemisphere mean trends, Clim. Past, 19, 1481–1506, https://doi.org/10.5194/cp-19-1481-2023, 2023.

Hoffman, J. S., Clark, P. U., Parnell, A. C., and He, F.: Regional and global sea-surface temperatures during the last interglaciation,

Science, 355, 276–279, https://doi.org/10.1126/science.aai8464, 2017.

Hugelius, G., Strauss, J., Zubrzycki, S., Harden, J. W., Schuur, E. A. G., Ping, C.-L., Schirrmeister, L., Grosse, G., Michaelson, G. J., Koven, C. D., O'Donnell, J. A., Elberling, B., Mishra, U., Camill, P., Yu, Z., Palmtag, J., and Kuhry, P.: Estimated stocks of circumpolar permafrost carbon with quantified uncertainty ranges and identified data gaps, Biogeosciences, 11, 6573–6593, https://doi.org/10.5194/bg-11-6573-2014, 2014.

Jahn, A., Holland, M. M., and Kay, J. E.: Projections of an ice-free Arctic Ocean, Nature Reviews Earth & Environment, 5, 164–176, https://doi.org/10.1038/s43017-023-00515-9, 2024.

Jiang, X., Cai, H., and Yang, X.: Response of active layer thickening to wildfire in the pan-Arctic region: Permafrost type and vegetation type influences, Science of The Total Environment, 902, 166132, https://doi.org/10.1016/j.scitotenv.2023.166132, 2023.

Jones, M. C., Grosse, G., Treat, C., Turetsky, M., Anthony, K. W., and Brosius, L.: Past permafrost dynamics can inform future permafrost carbon-climate feedbacks, Communications Earth & Environment, 4, 1–13, https://doi.org/10.1038/s43247-023-00886-3, 2023.

Jones, M. K. W., Pollard, W. H., and Jones, B. M.: Rapid initialization of retrogressive thaw slumps in the Canadian high Arctic and their response to climate and terrain factors, Environmental Research Letters, 14, 055006, https://doi.org/10.1088/1748-9326/ab12fd, 2019.

Jorgenson, M. T., Kanevskiy, M., Shur, Y., Moskalenko, N., Brown, D. R. N., Wickland, K., Striegl, R., and Koch, J.: Role of ground ice dynamics and ecological feedbacks in recent ice wedge degradation and stabilization, Journal of Geophysical Research: Earth Surface, 120, 2280–2297, https://doi.org/10.1002/2015JF003602, 2015.

Kanevskiy, M., Shur, Y., Jorgenson, T., Brown, D. R., Moskalenko, N., Brown, J., Walker, D. A., Raynolds, M. K., and Buchhorn, M.: Degradation and stabilization of ice wedges: Implications for assessing risk of thermokarst in northern Alaska, Geomorphology, 297, 20–42, https://doi.org/10.1016/j.geomorph.2017.09.001, 2017.

Kaufman, D., McKay, N., Routson, C., Erb, M., Davis, B., Heiri, O., Jaccard, S., Tierney, J., Dätwyler, C., Axford, Y., Brussel, T., Cartapanis, O., Chase, B., Dawson, A., de Vernal, A., Engels, S., Jonkers, L., Marsicek, J., Moffa-Sánchez, P., Morrill, C., Orsi, A., Rehfeld, K., Saunders, K., Sommer, P. S., Thomas, E., Tonello, M., Tóth, M., Vachula, R., Andreev, A., Bertrand, S., Biskaborn, B., Bringué, M., Brooks, S., Caniupán, M., Chevalier, M., Cwynar, L., Emile-Geay, J., Fegyveresi, J., Feurdean, A., Finsinger, W., Fortin, M.-C., Foster, L., Fox, M., Gajewski, K., Grosjean, M., Hausmann, S., Heinrichs, M., Holmes, N., Ilyashuk, B., Ilyashuk, E., Juggins, S., Khider, D., Koinig, K., Langdon, P., Larocque-Tobler, I., Li, J., Lotter, A., Luoto, T., Mackay, A., Magyari, E., Malevich, S., Mark, B., Massaferro, J., Montade, V., Nazarova, L., Novenko, E., Pařil, P., Pearson, E., Peros, M., Pienitz, R., Płóciennik, M., Porinchu, D., Potito, A., Rees, A., Reinemann, S., Roberts, S., Rolland, N., Salonen, S., Self, A., Seppä, H., Shala, S., St-Jacques, J.-M., Stenni, B., Syrykh, L., Tarrats, P., Taylor, K., van den Bos, V., Velle, G., Wahl, E., Walker, I., Wilmshurst, J., Zhang, E., and Zhilich, S.: A global database of Holocene paleotemperature records, Sci-

entific Data, 7, 115, https://doi.org/10.1038/s41597-020-0445-3, 2020.

Kaufman, D. S. and Broadman, E.: Revisiting the Holocene global temperature conundrum, Nature, 614, 425–435, https://doi.org/10.1038/s41586-022-05536-w, 2023.

Kaushal, N., Lechleitner, F. A., Wilhelm, M., Azennoud, K., Bühler, J. C., Braun, K., Ait Brahim, Y., Baker, A., Burstyn, Y., Comas-Bru, L., Fohlmeister, J., Goldsmith, Y., Harrison, S. P., Hatvani, I. G., Rehfeld, K., Ritzau, M., Skiba, V., Stoll, H. M., Szűcs, J. G., Tanos, P., Treble, P. C., Azevedo, V., Baker, J. L., Borsato, A., Chawchai, S., Columbu, A., Endres, L., Hu, J., Kern, Z., Kimbrough, A., Koç, K., Markowska, M., Martrat, B., Masood Ahmad, S., Nehme, C., Novello, V. F., Pérez-Mejías, C., Ruan, J., Sekhon, N., Sinha, N., Tadros, C. V., Tiger, B. H., Warken, S., Wolf, A., Zhang, H., and SISAL Working Group members: SISALv3: a global speleothem stable isotope and trace element database, Earth Syst. Sci. Data, 16, 1933–1963, https://doi.org/10.5194/essd-16-1933-2024, 2024.

Kim, I.-W., Timmermann, A., Kim, J.-E., Rodgers, K. B., Lee, S.-S., Lee, H., and Wieder, W. R.: Abrupt increase in Arctic-Subarctic wildfires caused by future permafrost thaw, Nature Communications, 15, 7868, https://doi.org/10.1038/s41467-024-51471-x, 2024.

Klemm, J., Herzschuh, U., Pisaric, M. F. J., Telford, R. J., Heim, B., and Pestryakova, L. A.: A pollen-climate transfer function from the tundra and taiga vegetation in Arctic Siberia and its applicability to a Holocene record, Palaeogeography, Palaeoclimatology, Palaeoecology, 386, 702–713, https://doi.org/10.1016/j.palaeo.2013.06.033, 2013.

Köhler, P. and van de Wal, R. S. W.: Interglacials of the Quaternary defined by northern hemispheric land ice distribution outside of Greenland, Nature Communications, 11, 5124, https://doi.org/10.1038/s41467-020-18897-5, 2020.

Kokelj, S. V. and Jorgenson, M. T.: Advances in Thermokarst Research, Permafrost and Periglacial Processes, 24, 108–119, https://doi.org/10.1002/ppp.1779, 2013.

Kropp, H., Loranty, M. M., Natali, S. M., Kholodov, A. L., Rocha, A. V., Myers-Smith, I., Abbot, B. W., Abermann, J., Blanc-Betes, E., Blok, D., Blume-Werry, G., Boike, J., Breen, A. L., Cahoon, S. M. P., Christiansen, C. T., Douglas, T. A., Epstein, H. E., Frost, G. V., Goeckede, M., Høye, T. T., Mamet, S. D., O'Donnell, J. A., Olefeldt, D., Phoenix, G. K., Salmon, V. G., Sannel, A. B. K., Smith, S. L., Sonnentag, O., Vaughn, L. S., Williams, M., Elberling, B., Gough, L., Hjort, J., Lafleur, P. M., Euskirchen, E. S., Heijmans, M. M., Humphreys, E. R., Iwata, H., Jones, B. M., Jorgenson, M. T., Grünberg, I., Kim, Y., Laundre, J., Mauritz, M., Michelsen, A., Schaepman-Strub, G., Tape, K. D., Ueyama, M., Lee, B.-Y., Langley, K., and Lund, M.: Shallow soils are warmer under trees and tall shrubs across Arctic and Boreal ecosystems, Environmental Research Letters, 16, 015001, https://doi.org/10.1088/1748-9326/abc994, 2020.

Kwiecien, O., Braun, T., Brunello, C. F., Faulkner, P., Hausmann, N., Helle, G., Hoggarth, J. A., Ionita, M., Jazwa, C. S., Kelmelis, S., Marwan, N., Nava-Fernandez, C., Nehme, C., Opel, T., Oster, J. L., Perşoiu, A., Petrie, C., Prufer, K., Saarni, S. M., Wolf, A., and Breitenbach, S. F. M.: What we talk about when we talk about seasonality – A transdisciplinary review, Earth-Sci. Rev., 225, 103843, https://doi.org/10.1016/j.earscirev.2021.103843, 2022.

Lachenbruch, A. H.: Mechanics of Thermal Contraction Cracks and Ice-Wedge Polygons in Permafrost, in: Geological Society of America Special Papers, Geological Society of America, vol. 70, 1–66, https://doi.org/10.1130/SPE70-p1, 1962.

Langer, M., Nitzbon, J., Groenke, B., Assmann, L.-M., Schneider von Deimling, T., Stuenzi, S. M., and Westermann, S.: The evolution of Arctic permafrost over the last 3 centuries from ensemble simulations with the CryoGridLite permafrost model, The Cryosphere, 18, 363–385, https://doi.org/10.5194/tc-18-363-2024, 2024.

Lauriol, B., Ford, D. C., Cinq-Mars, J., and Morris, W. A.: The chronology of speleothem deposition in northern Yukon and its relationships to permafrost, Canadian Journal of Earth Sciences, 34, 902–911, https://doi.org/10.1139/e17-075, 1997.

Lauritzen, S.-E.: High-Resolution Paleotemperature Proxy Record for the Last Interglaciation Based on Norwegian Speleothems, Quaternary Research, 43, 133–146, https://doi.org/10.1006/qres.1995.1015, 1995.

Lauritzen, S.-E. and Lundberg, J.: Calibration of the speleothem delta function: an absolute temperature record for the Holocene in northern Norway, The Holocene, 9, 659–669, https://doi.org/10.1191/095968399667823929, 1999.

Lawrence, D. M., Slater, A. G., Tomas, R. A., Holland, M. M., and Deser, C.: Accelerated Arctic land warming and permafrost degradation during rapid sea ice loss, Geophys. Res. Lett., 35, https://doi.org/10.1029/2008GL033985, 2008.

Li, W., Tian, F., Rudaya, N., Herzschuh, U., and Cao, X.: Pollen-Based Holocene Thawing-History of Permafrost in Northern Asia and Its Potential Impacts on Climate Change, Frontiers in Ecology and Evolution, 10, https://doi.org/10.3389/fevo.2022.894471, 2022.

Liljedahl, A. K., Boike, J., Daanen, R. P., Fedorov, A. N., Frost, G. V., Grosse, G., Hinzman, L. D., Iijma, Y., Jorgenson, J. C., Matveyeva, N., Necsoiu, M., Raynolds, M. K., Romanovsky, V. E., Schulla, J., Tape, K. D., Walker, D. A., Wilson, C. J., Yabuki, H., and Zona, D.: Pan-Arctic ice-wedge degradation in warming permafrost and its influence on tundra hydrology, Nature Geoscience, 9, 312–318, https://doi.org/10.1038/ngeo2674, 2016.

Lindgren, A., Hugelius, G., and Kuhry, P.: Extensive loss of past permafrost carbon but a net accumulation into present-day soils, Nature, 560, 219–222, https://doi.org/10.1038/s41586-018-0371-0, 2018.

Liu, J., Zhang, T., Clow, G. D., and Jafarov, E.: Application of Tikhonov regularization to reconstruct past climate record from borehole temperature, Inverse Problems in Science and Engineering, 29, 3167–3189, https://doi.org/10.1080/17415977.2021.1975700, 2021.

Liu, Y. and Jiang, D.: Mid-Holocene permafrost: Results from CMIP5 simulations, Journal of Geophysical Research: Atmospheres, 121, 221–240, https://doi.org/10.1002/2015JD023837, 2016.

Löfverström, M., Caballero, R., Nilsson, J., and Kleman, J.: Evolution of the large-scale atmospheric circulation in response to changing ice sheets over the last glacial cycle, Clim. Past, 10, 1453–1471, https://doi.org/10.5194/cp-10-1453-2014, 2014.

Lyu, Z., Sommers, P., Schmidt, S. K., Magnani, M., Cimpoiasu, M., Kuras, O., Zhuang, Q., Oh, Y., De La Fuente, M., Cramm, M., and Bradley, J. A.: Seasonal dynamics of

Arctic soils: Capturing year-round processes in measurements and soil biogeochemical models, Earth-Sci. Rev., 254, 104820, https://doi.org/10.1016/j.earscirev.2024.104820, 2024.

Marcott, S. A., Shakun, J. D., Clark, P. U., and Mix, A. C.: A Reconstruction of Regional and Global Temperature for the Past 11,300 Years, Science, 339, 1198–1201, https://doi.org/10.1126/science.1228026, 2013.

Matsuoka, N., Christiansen, H. H., and Watanabe, T.: Ice-wedge polygon dynamics in Svalbard: Lessons from a decade of automated multi-sensor monitoring, Permafrost and Periglacial Processes, 29, 210–227, https://doi.org/10.1002/ppp.1985, 2018.

Müller-Ißberner, L. A., Nitzbon, J., and Dietze, E.: Compilation of speleothem growth records and hiatuses in the northern hemisphere (north of 20° N) for the mid Holocene (6 ka BP) and the last interglacial (127 ka BP), Zenodo [data set], https://doi.org/10.5281/zenodo.14512888, 2024.

Murton, J. B. and Kolstrup, E.: Ice-wedge casts as indicators of palaeotemperatures: precise proxy or wishful thinking?, Progress in Physical Geography: Earth and Environment, 27, 155–170, https://doi.org/10.1191/0309133303pp365ra, 2003.

Nicholson, S. L., Pike, A. W. G., Hosfield, R., Roberts, N., Sahy, D., Woodhead, J., Cheng, H., Edwards, R. L., Affolter, S., Leuenberger, M., Burns, S. J., Matter, A., and Fleitmann, D.: Pluvial periods in Southern Arabia over the last 1.1 million-years, Quaternary Science Reviews, 229, 106112, https://doi.org/10.1016/j.quascirev.2019.106112, 2020.

Nitzbon, J.: Interglacial permafrost dynamics: CryoGridLite.jl climate forcing data based on AWI-ESM-2 climate model output, Zenodo [data set], https://doi.org/10.5281/zenodo.14244199, 2024a.

Nitzbon, J.: Interglacial permafrost dynamics: CryoGridLite.jl model diagnostics, plotting and analysis scripts, Zenodo [code], https://doi.org/10.5281/zenodo.14243857, 2024b.

Nitzbon, J. and Langer, M.: Interglacial permafrost dynamics: CryoGridLite.jl model source code and parameter input file, Zenodo [code], https://doi.org/10.5281/zenodo.14243849, 2024.

Nitzbon, J., Krinner, G., Schneider von Deimling, T., Werner, M., and Langer, M.: First Quantification of the Permafrost Heat Sink in the Earth's Climate System, Geophys. Res. Lett., 50, e2022GL102053, https://doi.org/10.1029/2022GL102053, 2023.

Nitzbon, J., Schneider von Deimling, T., Aliyeva, M., Chadburn, S. E., Grosse, G., Laboor, S., Lee, H., Lohmann, G., Steinert, N. J., Stuenzi, S. M., Werner, M., Westermann, S., and Langer, M.: No respite from permafrost-thaw impacts in the absence of a global tipping point, Nature Climate Change, 14, 573–585, https://doi.org/10.1038/s41558-024-02011-4, 2024.

Obu, J., Westermann, S., Bartsch, A., Berdnikov, N., Christiansen, H. H., Dashtseren, A., Delaloye, R., Elberling, B., Etzelmüller, B., Kholodov, A., Khomutov, A., Kääb, A., Leibman, M. O., Lewkowicz, A. G., Panda, S. K., Romanovsky, V., Way, R. G., Westergaard-Nielsen, A., Wu, T., Yamkhin, J., and Zou, D.: Northern Hemisphere permafrost map based on TTOP modelling for 2000–2016 at 1 km2 scale, Earth-Sci. Rev., 193, 299–316, https://doi.org/10.1016/j.earscirev.2019.04.023, 2019.

O'ishi, R., Chan, W.-L., Abe-Ouchi, A., Sherriff-Tadano, S., Ohgaito, R., and Yoshimori, M.: PMIP4/CMIP6 last interglacial simulations using three different versions of MIROC: importance of vegetation, Clim. Past, 17, 21–36, https://doi.org/10.5194/cp-17-21-2021, 2021.

Opel, T., Bertran, P., Grosse, G., Jones, M., Luetscher, M., Schirrmeister, L., Stadelmaier, K. H., and Veremeeva, A.: Ancient permafrost and past permafrost in the Northern Hemisphere, in: Reference Module in Earth Systems and Environmental Sciences, Elsevier, ISBN 978-0-12-409548-9, https://doi.org/10.1016/B978-0-323-99931-1.00258-0, 2024.

Osman, M. B., Tierney, J. E., Zhu, J., Tardif, R., Hakim, G. J., King, J., and Poulsen, C. J.: Globally resolved surface temperatures since the Last Glacial Maximum, Nature, 599, 239–244, https://doi.org/10.1038/s41586-021-03984-4, 2021.

Otto-Bliesner, B. L., Braconnot, P., Harrison, S. P., Lunt, D. J., Abe-Ouchi, A., Albani, S., Bartlein, P. J., Capron, E., Carlson, A. E., Dutton, A., Fischer, H., Goelzer, H., Govin, A., Haywood, A., Joos, F., LeGrande, A. N., Lipscomb, W. H., Lohmann, G., Mahowald, N., Nehrbass-Ahles, C., Pausata, F. S. R., Peterschmitt, J.-Y., Phipps, S. J., Renssen, H., and Zhang, Q.: The PMIP4 contribution to CMIP6 – Part 2: Two interglacials, scientific objective and experimental design for Holocene and Last Interglacial simulations, Geosci. Model Dev., 10, 3979–4003, https://doi.org/10.5194/gmd-10-3979-2017, 2017.

Otto-Bliesner, B. L., Brady, E. C., Zhao, A., Brierley, C. M., Axford, Y., Capron, E., Govin, A., Hoffman, J. S., Isaacs, E., Kageyama, M., Scussolini, P., Tzedakis, P. C., Williams, C. J. R., Wolff, E., Abe-Ouchi, A., Braconnot, P., Ramos Buarque, S., Cao, J., de Vernal, A., Guarino, M. V., Guo, C., LeGrande, A. N., Lohmann, G., Meissner, K. J., Menviel, L., Morozova, P. A., Nisancioglu, K. H., O'ishi, R., Salas y Mélia, D., Shi, X., Sicard, M., Sime, L., Stepanek, C., Tomas, R., Volodin, E., Yeung, N. K. H., Zhang, Q., Zhang, Z., and Zheng, W.: Large-scale features of Last Interglacial climate: results from evaluating the *lig127k* simulations for the Coupled Model Intercomparison Project (CMIP6)–Paleoclimate Modeling Intercomparison Project (PMIP4), Clim. Past, 17, 63–94, https://doi.org/10.5194/cp-17-63-2021, 2021.

Pollack, H. N. and Huang, S.: Climate Reconstruction from Subsurface Temperatures, Annual Review of Earth and Planetary Sciences, 28, 339–365, https://doi.org/10.1146/annurev.earth.28.1.339, 2000.

Rantanen, M., Karpechko, A. Y., Lipponen, A., Nordling, K., Hyvärinen, O., Ruosteenoja, K., Vihma, T., and Laaksonen, A.: The Arctic has warmed nearly four times faster than the globe since 1979, Communications Earth & Environment, 3, 1–10, https://doi.org/10.1038/s43247-022-00498-3, 2022.

Reyes, A. V., Froese, D. G., and Jensen, B. J.: Permafrost response to last interglacial warming: field evidence from non-glaciated Yukon and Alaska, Quaternary Science Reviews, 29, 3256–3274, https://doi.org/10.1016/j.quascirev.2010.07.013, 2010.

Riseborough, D. W., Shiklomanov, N., Etzelmüller, B., Gruber, S., and Marchenko, S.: Recent advances in permafrost modelling, Permafrost and Periglacial Processes, 19, 137–156, https://doi.org/10.1002/ppp.615, 2008.

Saito, K., Okuno, J., Machiya, H., Iwahana, G., Ohno, H., and Yokohata, T.: Climatic assessment of circum-Arctic permafrost zonation over the last 122 kyr, Polar Science, 31, 100765, https://doi.org/10.1016/j.polar.2021.100765, 2022.

Schirrmeister, L., Fuchs, M. C., Opel, T., Andreev, A., Kienast, F., Schneider, A., Nazarova, L., Frolova, L., Kuzmina, S., Kuznetsova, T., Tumskoy, V., Matthes, H., Lohmann, G., Grosse, G., Kunitsky, V., Meyer, H., Zimmermann, H. H., Herzschuh, U., Böhmer, T., Umbo, S., Modestou, S., Breitenbach, S. F. M.,

Pismeniuk, A., Schwamborn, G., Kusch, S., and Wetterich, S.: Newly dated permafrost deposits and their paleoecological inventory reveal an Eemian much warmer than today in Arctic Siberia, Clim. Past, 21, 1143–1184, https://doi.org/10.5194/cp-21-1143-2025, 2025.

Shi, X., Lohmann, G., Sidorenko, D., and Yang, H.: Early-Holocene simulations using different forcings and resolutions in AWI-ESM, The Holocene, 30, 996–1015, https://doi.org/10.1177/0959683620908634, 2020.

Shi, X., Werner, M., Wang, Q., Yang, H., and Lohmann, G.: Simulated Mid-Holocene and Last Interglacial Climate Using Two Generations of AWI-ESM, Journal of Climate, 35, 7811–7831, https://doi.org/10.1175/JCLI-D-22-0354.1, 2022.

Sidorenko, D., Goessling, H., Koldunov, N., Scholz, P., Danilov, S., Barbi, D., Cabos, W., Gurses, O., Harig, S., Hinrichs, C., Juricke, S., Lohmann, G., Losch, M., Mu, L., Rackow, T., Rakowsky, N., Sein, D., Semmler, T., Shi, X., Stepanek, C., Streffing, J., Wang, Q., Wekerle, C., Yang, H., and Jung, T.: Evaluation of FESOM2.0 Coupled to ECHAM6.3: Preindustrial and HighResMIP Simulations, Journal of Advances in Modeling Earth Systems, 11, 3794–3815, https://doi.org/10.1029/2019MS001696, 2019.

Spötl, C., Baker, J. L., Skiba, V., Honiat, A., Fohlmeister, J., Luetscher, M., and Trüssel, M.: Speleothems in subglacial caves: An emerging archive of glacial climate history and mountain glacier dynamics, Quaternary Science Reviews, 333, 108684, https://doi.org/10.1016/j.quascirev.2024.108684, 2024.

Stadelmaier, K. H., Ludwig, P., Bertran, P., Antoine, P., Shi, X., Lohmann, G., and Pinto, J. G.: A new perspective on permafrost boundaries in France during the Last Glacial Maximum, Clim. Past, 17, 2559–2576, https://doi.org/10.5194/cp-17-2559-2021, 2021.

Steinert, N. J., Debolskiy, M. V., Burke, E. J., García-Pereira, F., and Lee, H.: Evaluating permafrost definitions for global permafrost area estimates in CMIP6 climate models, Environmental Research Letters, 19, 014033, https://doi.org/10.1088/1748-9326/ad10d7, 2023.

Stuenzi, S. M., Kruse, S., Boike, J., Herzschuh, U., Oehme, A., Pestryakova, L. A., Westermann, S., and Langer, M.: Thermohydrological Impact of Forest Disturbances on Ecosystem-Protected Permafrost, Journal of Geophysical Research: Biogeosciences, 127, e2021JG006630, https://doi.org/10.1029/2021JG006630, 2022.

Tesi, T., Muschitiello, F., Smittenberg, R. H., Jakobsson, M., Vonk, J. E., Hill, P., Andersson, A., Kirchner, N., Noormets, R., Dudarev, O., Semiletov, I., and Gustafsson, O.: Massive remobilization of permafrost carbon during post-glacial warming, Nature Communications, 7, 13653, https://doi.org/10.1038/ncomms13653, 2016.

Treat, C. C., Kleinen, T., Broothaerts, N., Dalton, A. S., Dommain, R., Douglas, T. A., Drexler, J. Z., Finkelstein, S. A., Grosse, G., Hope, G., Hutchings, J., Jones, M. C., Kuhry, P., Lacourse, T., Lähteenoja, O., Loisel, J., Notebaert, B., Payne, R. J., Peteet, D. M., Sannel, A. B. K., Stelling, J. M., Strauss, J., Swindles, G. T., Talbot, J., Tarnocai, C., Verstraeten, G., Williams, C. J., Xia, Z., Yu, Z., Väliranta, M., Hättestrand, M., Alexanderson, H., and Brovkin, V.: Widespread global peatland establishment and persistence over the last 130 000 y, Proceedings of the National Academy of Sciences, 116, 4822–4827, https://doi.org/10.1073/pnas.1813305116, 2019.

Umbo, S., Panitz, S., Homann, J., McCoy, J., Pound, M., Opel, T., Lechleitner, F., Vaks, A., Osintzev, A., Adrian, I., Kononov, A., and Breitenbach, S. F. M.: Late Miocene speleothems show significant warming, temperate vegetation, and wildfires in Arctic Siberia, Scientific Reports, 15, 28420, https://doi.org/10.1038/s41598-025-12287-x, 2025.

Vaks, A., Gutareva, O. S., Breitenbach, S. F. M., Avirmed, E., Mason, A. J., Thomas, A. L., Osinzev, A. V., Kononov, A. M., and Henderson, G. M.: Speleothems Reveal 500 000-Year History of Siberian Permafrost, Science, 340, 183–186, https://doi.org/10.1126/science.1228729, 2013.

Vaks, A., Mason, A. J., Breitenbach, S. F. M., Kononov, A. M., Osinzev, A. V., Rosensaft, M., Borshevsky, A., Gutareva, O. S., and Henderson, G. M.: Palaeoclimate evidence of vulnerable permafrost during times of low sea ice, Nature, 577, 221–225, https://doi.org/10.1038/s41586-019-1880-1, 2020.

Vandenberghe, J., French, H. M., Gorbunov, A., Marchenko, S., Velichko, A. A., Jin, H., Cui, Z., Zhang, T., and Wan, X.: The Last Permafrost Maximum (LPM) map of the Northern Hemisphere: permafrost extent and mean annual air temperatures, 25–17 ka BP, Boreas, 43, 652–666, https://doi.org/10.1111/bor.12070, 2014.

van Vliet-Lanoë, B. and Lisitsyna, O.: Permafrost Extent at the Last Glacial Maximum and at the Holocene Optimum. the Climex Map, in: Permafrost Response on Economic Development, Environmental Security and Natural Resources, edited by: Paepe, R., Melnikov, V. P., Van Overloop, E., and Gorokhov, V. D., Springer Netherlands, Dordrecht, 215–225, ISBN 978-94-010-0684-2, https://doi.org/10.1007/978-94-010-0684-2_14, 2001.

Vermassen, F., O'Regan, M., de Boer, A., Schenk, F., Razmjooei, M., West, G., Cronin, T. M., Jakobsson, M., and Coxall, H. K.: A seasonally ice-free Arctic Ocean during the Last Interglacial, Nature Geoscience, 16, 723–729, https://doi.org/10.1038/s41561-023-01227-x, 2023.

Walter Anthony, K. M., Anthony, P., Hasson, N., Edgar, C., Sivan, O., Eliani-Russak, E., Bergman, O., Minsley, B. J., James, S. R., Pastick, N. J., Kholodov, A., Zimov, S., Euskirchen, E., Bret-Harte, M. S., Grosse, G., Langer, M., and Nitzbon, J.: Upland Yedoma taliks are an unpredicted source of atmospheric methane, Nature Communications, 15, 6056, https://doi.org/10.1038/s41467-024-50346-5, 2024.

Willeit, M. and Ganopolski, A.: Coupled Northern Hemisphere permafrost–ice-sheet evolution over the last glacial cycle, Clim. Past, 11, 1165–1180, https://doi.org/10.5194/cp-11-1165-2015, 2015.

Winkelmann, R., Dennis, D. P., Donges, J. F., Loriani, S., Klose, A. K., Abrams, J. F., Alvarez-Solas, J., Albrecht, T., Armstrong McKay, D., Bathiany, S., Blasco Navarro, J., Brovkin, V., Burke, E., Danabasoglu, G., Donner, R. V., Drüke, M., Georgievski, G., Goelzer, H., Harper, A. B., Hegerl, G., Hirota, M., Hu, A., Jackson, L. C., Jones, C., Kim, H., Koenigk, T., Lawrence, P., Lenton, T. M., Liddy, H., Licón-Saláiz, J., Menthon, M., Montoya, M., Nitzbon, J., Nowicki, S., Otto-Bliesner, B., Pausata, F., Rahmstorf, S., Ramin, K., Robinson, A., Rockström, J., Romanou, A., Sakschewski, B., Schädel, C., Sherwood, S., Smith, R. S., Steinert, N. J., Swingedouw, D., Willeit, M., Weijer, W., Wood, R., Wyser, K., and Yang, S.: The Tipping Points Modelling Intercomparison Project (TIPMIP): Assessing tipping point risks in the Earth system, EGUsphere [preprint], https://doi.org/10.5194/egusphere-2025-1899, 2025.

Wolfe, S. A., Morse, P. D., Neudorf, C. M., Kokelj, S. V., Lian, O. B., and O'Neill, H. B.: Contemporary sand wedge development in seasonally frozen ground and paleoenvironmental implications, Geomorphology, 308, 215–229, https://doi.org/10.1016/j.geomorph.2018.02.015, 2018.

Yan, X., Zhang, X., Liu, B., Mithan, H. T., Hellstrom, J., Nuber, S., Drysdale, R., Wu, J., Lin, F., Zhao, N., Zhang, Y., Kang, W., and Liu, J.: Asynchronicity of deglacial permafrost thawing controlled by millennial-scale climate variability, Nature Communications, 16, 290, https://doi.org/10.1038/s41467-024-55184-z, 2025.

Žák, K., Richter, D. K., Filippi, M., Živor, R., Deininger, M., Mangini, A., and Scholz, D.: Coarsely crystalline cryogenic cave carbonate – a new archive to estimate the Last Glacial minimum permafrost depth in Central Europe, Clim. Past, 8, 1821–1837, https://doi.org/10.5194/cp-8-1821-2012, 2012.

Zhang, T., Heginbottom, J. A., Barry, R. G., and Brown, J.: Further statistics on the distribution of permafrost and ground ice in the Northern Hemisphere 1, Polar Geography, 24, 126–131, https://doi.org/10.1080/10889370009377692, 2000.

Zhang, X., Lohmann, G., Knorr, G., and Xu, X.: Different ocean states and transient characteristics in Last Glacial Maximum simulations and implications for deglaciation, Clim. Past, 9, 2319–2333, https://doi.org/10.5194/cp-9-2319-2013, 2013.

Zoltai, S.: Permafrost Distribution in Peatlands of West-Central Canada During the Holocene Warm Period 6000 Years BP, Géographie Physique et Quaternaire, 49, 45–54, https://doi.org/10.7202/033029ar, 1995.